Geochemistry, Geophysics, Geosystems®

AGU ADVANCING EARTH AND SPACE SCIENCES

RESEARCH ARTICLE
10.1029/2024GC011491

Magmatic Storage and Volatile Fluxes of the 2021 La Palma Eruption

K. Dayton[1], E. Gazel[1], P. E. Wieser[2], V. R. Troll[3,4,5], J. C. Carracedo[5], M. Aulinas[6,7], and F. J. Perez-Torrado[5]

[1]Department of Earth and Atmospheric Sciences, Cornell University, Ithaca, NY, USA, [2]Department of Earth and Planetary Sciences, University of California Berkeley, Berkeley, CA, USA, [3]Department of Earth Sciences, Section for Natural Resources and Sustainable Development, Uppsala University, Uppsala, Sweden, [4]Centre of Natural Hazards and Disaster Science (CNDS), Uppsala University, Uppsala, Sweden, [5]Instituto de Estudios Ambientales y Recursos Naturales (i-UNAT), University of Las Palmas de Gran Canaria (ULPGC), Las Palmasde Gran Canaria, Spain, [6]Department of Mineralogia, Petrologia, i Geologia Aplicada, Facultat Ciències de la Terra, Universitat de Barcelona, Barcelona, Spain, [7]Geomodels Research Institute, University of Barcelona, Barcelona, Spain

Key Points:

- Melt and fluid inclusion record sub-Moho storage depths
- Melt inclusions from the same crystal population can lose up to 1.5 wt% H_2O within a single eruption through diffusive re-equilibration during magma replenishment
- Heterogeneous abundances of volatiles in melt inclusion populations reflect pre-eruptive fractional crystallization

Supporting Information:

Supporting Information may be found in the online version of this article.

Correspondence to:

E. Gazel,
egazel@cornell.edu

Citation:

Dayton, K., Gazel, E., Wieser, P. E., Troll, V. R., Carracedo, J. C., Aulinas, M., & Perez-Torrado, F. J. (2024). Magmatic storage and volatile fluxes of the 2021 La Palma eruption. *Geochemistry, Geophysics, Geosystems*, *25*, e2024GC011491. https://doi.org/10.1029/2024GC011491

Received 2 FEB 2024
Accepted 29 MAY 2024
Corrected 10 JUL 2024

This article was corrected on 10 JUL 2024. See the end of the full text for details.

Author Contributions:

Conceptualization: K. Dayton, E. Gazel
Data curation: K. Dayton
Formal analysis: K. Dayton
Funding acquisition: E. Gazel
Investigation: K. Dayton, E. Gazel
Methodology: K. Dayton, E. Gazel, P. E. Wieser, V. R. Troll, J. C. Carracedo
Project administration: E. Gazel
Resources: E. Gazel, V. R. Troll, J. C. Carracedo, F. J. Perez-Torrado
Software: P. E. Wieser

Abstract The 2021 La Palma eruption (Tajogaite) was unprecedented in magnitude, duration, and degree of monitoring compared to historical volcanism on La Palma. Here, we provide data on melt inclusions in samples from the beginning and end of the eruption to compare the utility of both melt and fluid inclusions as recorders of magma storage. We also investigated compositional heterogeneities within the magmatic plumbing system. We found two populations of olivine crystals: a low Mg# (78–82) population present at the beginning and end of eruption, recording the maximum volatile contents (2.5 wt % H_2O, 1,800 ppm F, 700 ppm Cl, 3,800 ppm S) and a higher Mg# (83–86) population sampled toward the end of the eruption, with lower volatile contents. Despite their host composition, melt inclusions share the same maximum range of CO_2 concentrations (1.2–1.4 wt %), indicating olivine growth and inclusion capture at similar depths. Overall, both melt and fluid inclusions record similar pressures (450–850 MPa, ∼15–30 km), and when hosted in the same olivine crystal pressures are indistinguishable within error. At these mantle pressures, CO_2 is expected to be an exsolved phase explaining the similar range of CO_2 between the two samples, but other volatile species (F, Cl, S) behave incompatibly, and thus, the increase between the two olivine populations can be explained by fractional crystallization prior to eruption. Finally, based on our new data, we provide estimates on the total volatile emission of the eruption.

Plain Language Summary Melt inclusions, droplets of magma trapped during olivine crystal growth, record both evolved and primitive melts at the same depths exhumed during the 2021 Tajogaite eruption.

1. Introduction

The Canary Islands are part of the Canary hotspot track of the Central Eastern Atlantic and consist of seven main volcanic islands stretched over 500-km, sitting on Jurassic-aged oceanic crust (Carracdeo & Troll, 2016). These volcanic islands record a general westward age progression with La Palma and El Hierro subaerial volcanism being the youngest at ∼1.7 and 1.1 Ma, respectively (Carracedo et al., 2001). Multiple models of formation have been argued as an explanation for the existence of the Canary Islands, including a mantle plume, edge-driven convection, or a tectonically controlled fracture (Anguita & Hernán, 2000; Carracedo et al., 1998; Duggen et al., 2009; Geldmacher et al., 2005; King & Ritsema, 2000; Zaczek et al., 2015). In recent years, a combination of a mantle plume edge-driven convection toward the "cold" African craton explains the apparent weak age progression of the Canary Islands as well as historic volcanism on both sides of the archipelago (Manjón-Cabeza Córdoba & Ballmer, 2022; Negredo et al., 2022; Troll & Carracedo, 2016). Although isotope systematics suggest the presence of recycled materials in the Canary Islands source (Day & Hilton, 2020; Day et al., 2009, 2010, 2022; Thirlwall et al., 1997; Walowski et al., 2019), the role of recycled volatiles, specifically CO_2, has been under-investigated as a potential driver of eruptive activity (Aiuppa et al., 2021; Allison et al., 2021; Taracsák et al., 2019).

Historical volcanism (recorded since Spanish colonization in the late 1,400s) of the Canary Islands has been centered at the Cumbre Vieja Ridge (CVR) (Figures 1a–1c), with a volcanic event occurring somewhere in the archipelago every 30–40 years and an average event duration of 50 days (Carracedo et al., 2007; Longpré &

Supervision: E. Gazel, P. E. Wieser, F. J. Perez-Torrado
Validation: P. E. Wieser
Visualization: K. Dayton, E. Gazel, P. E. Wieser
Writing – original draft: K. Dayton, E. Gazel
Writing – review & editing: K. Dayton, E. Gazel, P. E. Wieser, V. R. Troll, J. C. Carracedo, M. Aulinas, F. J. Perez-Torrado

Felpeto, 2021; Troll & Carracedo, 2016). Typical historical Canary Island volcanism takes the form of monogenetic eruptions of mafic compositions with both effusive and explosive activity, simultaneously creating lava flows and tephra deposits from multiple vents aligned along fractures (Carracdeo et al., 1992, 2022; Longpré & Felpeto, 2021; Troll & Carracedo, 2016).

1.1. The 2021 La Palma (Tajogaite) Eruption

The 2021 Tajogaite-eruption on La Palma displays many characteristics of a typical Canary historical eruption mentioned above. Prior to the start of volcanic activity on 19 September 2021, unrest under the CVR had been detected following seismic swarms in 2017 and 2018 (Torres-González et al., 2020). An increase in helium isotopic ratios and CO_2 emissions indicated a mantle-sourced magmatic intrusion, placed at 25 km 4 years prior to the start of eruptive activity (Torres-González et al., 2020). Following the start of seismic unrest in 2017, La Palma experienced nine seismic swarms prior to the final seismic event which began 8 days before the eruption start (Fernandez et al., 2022; Longpré, 2021). Pre-eruptive activity starting on 11 September has been interpreted as magmatic injection or underplating in a sill-like body at 7–10 km, which then transitioned to vertical dike motion as the path was cleared for vent opening on 19 September (D'Auria et al., 2022; Del Fresno et al., 2023; De Luca et al., 2022). Propagation of both sills and dikes led to the shallowing of earthquake hypocenters immediately prior to eruption (as also observed in the 2011–2012 Tagoro eruption off El Hierro) (López et al., 2012; Martí et al., 2013). Dike complexes, like those which fed the 2021 eruption, are exposed in eroded sections of the rift zones and are the main mechanisms of oceanic island growth (Carracedo, 1994; Carracedo et al., 2011; Delcamp et al., 2012).

When compared to the last two previous on-island eruptions of Cumbre Vieja in 1949 (378 days, volume of 44×10^6 m^3) and 1971 (245 days, volume of 46×10^6 m^3), the 2021 eruption was twice as long (85 days) and emitted an order of magnitude more material with a total volume of $253.9 \pm 6.9 \times 10^6$ m^3 (Civico et al., 2022) (Figure 1c). Ash emission from the eruption was significant and long-lasting, reaching all Canary Islands, mainland Europe, and even Barbados (Gaston et al., 2022). Plume heights reached up to 8.5 km with an average of 3.5 km above sea level visible from Tenerife (Carracedo et al., 2022). Explosivity of the 2021 eruption was also significant and variable, with multiple vents active simultaneously each displaying various behavior ranging from pulsating strombolian blasts to effusive lava flows (Bonadonna et al., 2022; Carracedo et al., 2022).

The 2021 lavas exhibit a compositional hybrid nature. Initially, they displayed a tephritic composition characterized by low MgO (~6 wt%) and TiO_2 (~4 wt%). As the eruption progressed, the lavas became increasingly mafic, reaching a consistently basanitic composition with higher MgO (~8 wt%) and lower TiO_2 (3.7 wt%) around day 20 (Day et al., 2022). Recent investigations into Sr and Os isotopes have identified the tapping of a more primitive reservoir during progression of the eruption (Day et al., 2022; Gonzalez-Garcia et al., 2023; Ubide et al., 2023). The process of the initial eruption involving a more fractionated magma is not unique to the 2021 event. In both the 1949 and 1971 eruptions, lower-MgO amphibole-bearing products erupted before basanites, suggesting fractionation as a widespread process beneath the Cumbre Vieja Ridge (Barker et al., 2015; Klügel et al., 2000). Although exhibiting temporal and compositional variability, a homogeneous asthenospheric magma source with a constant degree of 2.5%–3% partial melting has been proposed as the primary feeding source for the eruption, with modification by fractional crystallization (Day et al., 2022; Gonzalez-Garcia et al., 2023).

Because of the explosive activity and deposition of substantial quantities of tephra containing large, euhedral olivine phenocrysts, the 2021 eruption provides ideal conditions for studying melt inclusions due to the small size of tephra clasts, and, therefore, fast quench time minimizing post-eruptive modification (Lloyd et al., 2012). Melt inclusions, tiny droplets of melt trapped during crystal growth, are a powerful tool to understand the drivers and evolution of magmatic eruptions (Allison et al., 2021; Cashman et al., 2017; DeVitre, Gazel, et al., 2023; Hauri, 2002; Kent, 2008; Lowenstern, 1995; Metrich & Wallace, 2008; Moore et al., 2015, 2021; Rasmussen et al., 2018; Roedder, 1979; Wieser et al., 2021) (Figure 2). Though ideally able to preserve valuable information about magmatic processes prior to eruption, melt inclusions are subject to several, simultaneously occurring, post-entrapment processes. These processes include olivine crystallization on melt inclusion walls and subsequent Mg-Fe diffusive re-equilibration, also known as post-entrapment crystallization (PEC) (Danyushevsky et al., 2000; Esposito et al., 2012). H_2O loss from trapped melt upon ascent and clast-cooling (Lloyd et al., 2012), melt inclusion vapor bubble formation (Moore et al., 2015; Rasmussen et al., 2020; Wallace et al., 2015), and carbonate crystallization on vapor bubble walls (Moore et al., 2015, 2021; Venugopal et al., 2020) are also common post-

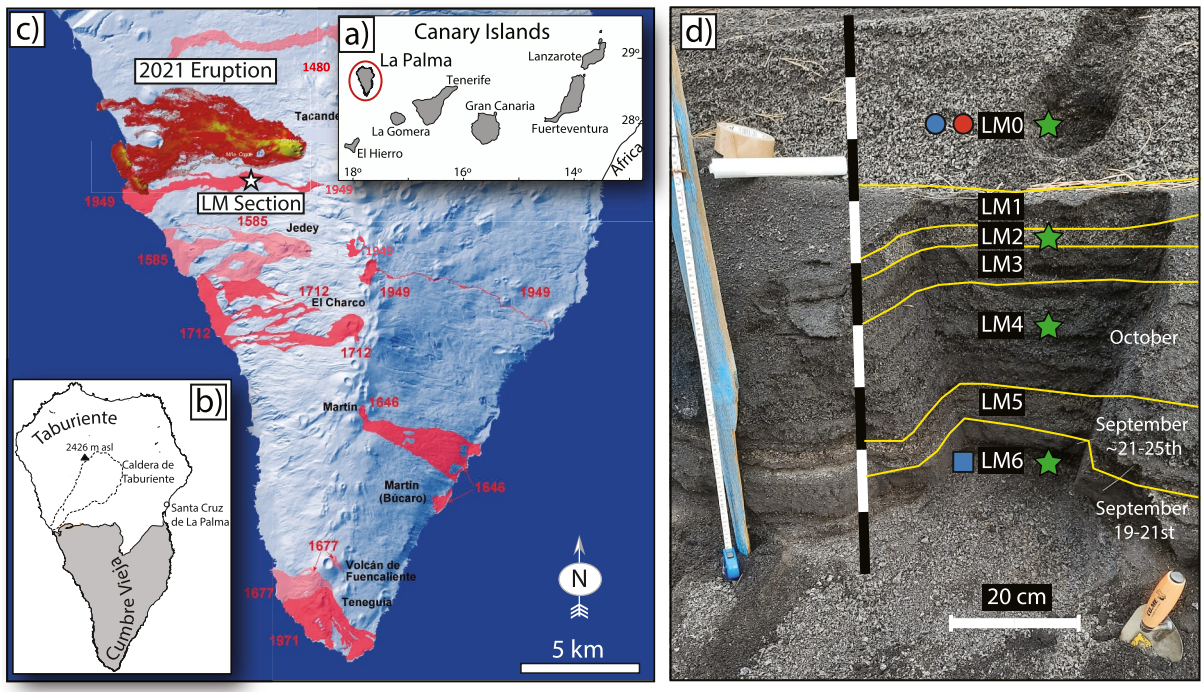

Figure 1. Geographic overview and sample collection. (a) The Canary Islands, with La Palma circled. (b) Simple geologic stages of La Palma, with the younger Cumbre Vieja ridge extending south from the older and extinct Taburiente shield volcano. (c) Historical volcanism of La Palma modified from Carracedo et al. (2022). Sample locations marked with a white star. (d) Stratigraphic section collected from the middle of road LP-212 on 17th January 2022 in Las Manchas (28.606552°N, −17.878136°W) following the conclusion of the 2021 eruption. The blue square and red circle indicate samples with melt inclusion data included in this work. Green stars indicate samples with fluid inclusion data published by Dayton et al. (2023). Dates of samples are derived from the stratigraphic column of Romero et al. (2022).

entrapment processes. Additionally, analytical challenges can also obscure the true volatile contents of melt inclusions. Uncalibrated Raman analysis of melt inclusion vapor bubbles within the CO_2 miscibility gap (ρCO_2 = 0.2–0.7 g/cm^3) below the critical point of CO_2 (~31.1°C) can lead to underestimates of CO_2 density in melt inclusion vapor bubbles leading to errors in saturation pressure calculations of up to 6 km (DeVitre, Dayton, et al., 2023). Here, we use the most recent best practices of melt-inclusion analysis to ensure the most accurate estimates of saturation pressure by hand-picking single crystals from fine-grained tephra and avoiding melt inclusions with anomalously high bubble-volume fractions that indicate obvious heterogenous entrapment (Steele-MacInnis et al., 2017). We also avoided melt inclusions with carbonates on the bubble walls and measured melt inclusions in the third dimension using Raman spectroscopy. Lastly, we analyzed melt-inclusion vapor bubbles above the critical point of CO_2 using calibrated Raman spectroscopy (DeVitre, Dayton, et al., 2023; DeVitre, Gazel, et al., 2023; DeVitre et al., 2021; Hanyu et al., 2020; Mironov et al., 2020; Rose-Koga et al., 2021).

From our previous work using fluid-inclusion barometry (Dayton et al., 2023), we constrained the magma storage at mantle depths prior to the 2021 eruption (15–27 km). In an attempt to comprehensively examine the geochemical processes and investigate the drivers of volcanism in the Canary Islands, we have now analyzed melt inclusions (glass plus vapor bubbles) and matrix glasses from the start (September, LM6) and end (December, LM0) of the 2021 eruption. We obtain volatile budgets of the mantle source that feeds the 2021 eruption and further constrain the magmatic plumbing system of Cumbre Vieja by identifying heterogeneities in volatile concentrations during the eruptive event. Specifically, we report volatile contents (H_2O, CO_2, fluorine, chlorine, sulfur) and major and trace element data on melt inclusions as well as whole rock data on the stratigraphic section used in Dayton et al. (2023) (Figure 1d). We analyze multiple melt inclusions (up to six) within the same olivine crystal (e.g., Figure 2b) to elucidate heterogenous entrapment (cf. Steele-MacInnis et al., 2017) of exsolved CO_2 fluid during melt inclusion capture, which can result in erroneously high CO_2 contents and saturation pressures if not properly identified. We compare our results to previously published fluid inclusion data from the same samples (Dayton et al., 2023), and analyzed both melt and fluid inclusions within the same crystals (Figures 2c

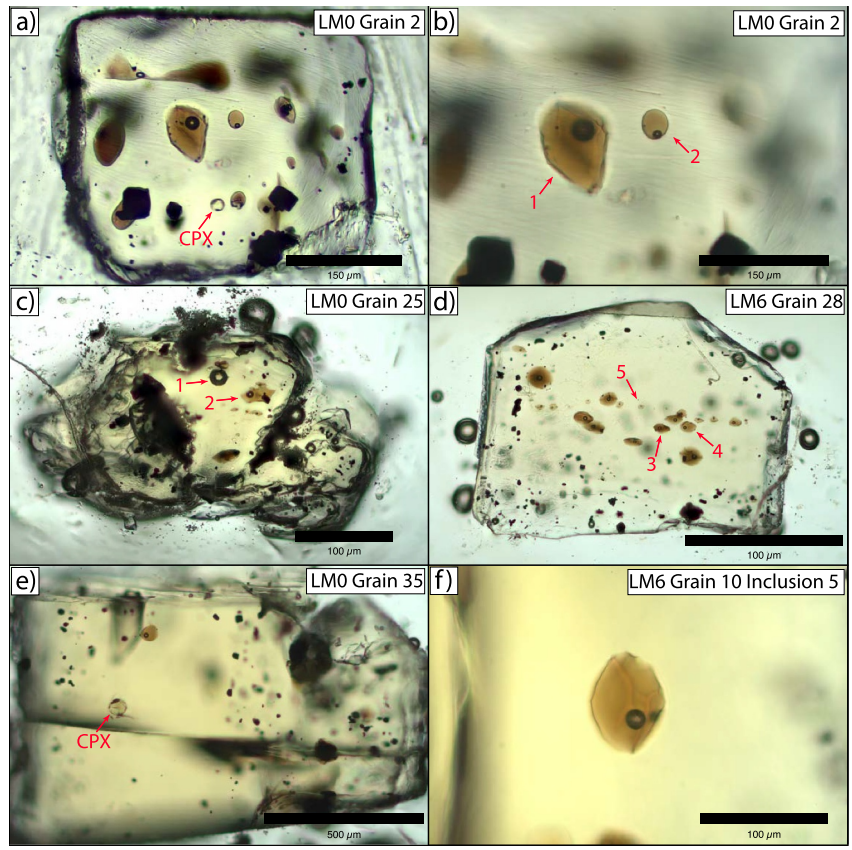

Figure 2. Melt Inclusion Photomicrographs (note: these are focus stacked images to allow inclusions at different depths to be visible within a single image). (a) LM0 Grain 2 with a clinopyroxene (CPX) inclusion and two analyzed melt inclusions in the grain center. (b) Magnified view of inclusions one and two in panel (a). (c) LM0 Grain 25 containing both fluid and melt inclusions. This grain is polished down the a-axis to give a "side" view of melt inclusions. Inclusion 2 is heterogeneously entrapped. (d) LM6 Grain 28 contains multiple inclusion assemblages recording different pressures. (e) LM0 G35 grain contains both a melt inclusion and clinopyroxene (CPX) inclusion trapped prior to oxide crystallization. (f) LM6 Grain 10 Inclusion five. Typical morphology of melt inclusions selected for analysis.

and 2d) to constrain magmatic processes and directly compare melt and fluid inclusion to investigate their utility and reliability as recorders of magma storage location.

2. Materials and Methods

Samples were collected from a stratigraphic section containing the entirety of 2021 eruptive deposit (Figure 1d). Sample LM6 represents the first 3 days of eruptive activity (September 19 to ~21) (Romero et al., 2022), while LM0 represents the final eruptive unit (~December). Olivine crystals were hand-picked, and individually polished to identify melt and fluid inclusions. CO_2 densities of melt inclusion vapor bubbles and fluid inclusions were collected via Raman spectroscopy in the Department of Earth and Atmospheric Sciences at Cornell University. Volatiles in exposed glass of melt inclusions were analyzed by secondary ion mass spectrometry (SIMS) in the Northeast National Ion Microprobe Facility at Woods Hole Oceanographic Institution, followed by major elements in the glass and host olivine by electron microprobe analyzer (EMPA) at the University of Massachusetts Amherst in the Department of Geosciences. Finally, both the glass and trace elements in olivine were collected by laser ablation induced coupled plasma mass spectrometry (LA-ICP-MS) in the Department of Earth and Atmospheric Sciences at Cornell University. Whole rock tephra data was collected via X-ray fluorescence (XRF) and induced coupled plasma mass spectrometry (ICP-MS) in the Peter Hooper GeoAnalytical Lab at Washington State University. Details on converting melt and fluid inclusion pressures are discussed at length in Supporting Information S1 and Data Set S1, along with more details on all materials and methods.

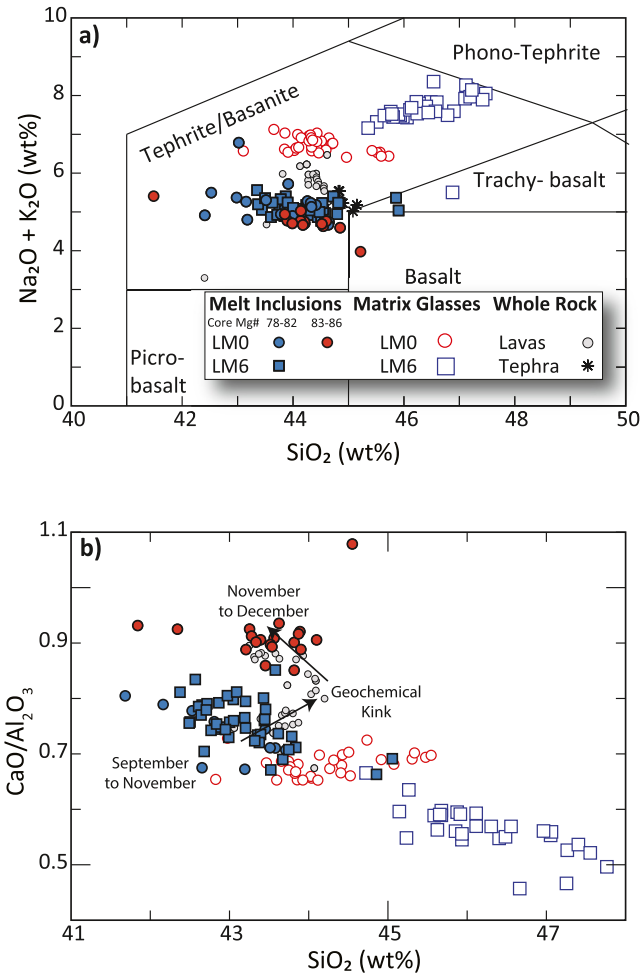

Figure 3. Major element (wt%) composition of melt inclusions and eruptive materials of the 2021 eruption. (a) Total Alkalis ($Na_2O + K_2O$) versus SiO_2 diagram (Le Bas et al., 1986) including melt inclusion and matrix glass from samples LM6 (September) and LM0 (December). Tephra (this work) and lava whole rock data (Day et al., 2022) span the entire Tajogaite eruption. (b) CaO/Al_2O_3 versus SiO_2 diagram identifying the "geochemical kink" in November 2021 and transition from fractionated, more evolved magma representing the start of the eruption to the more primitive composition present through the end of the eruption (Day et al., 2022; Gonzalez-Garcia et al., 2023; Ubide et al., 2023).

To calculate volatile fluxes, we use an estimates of the total emitted volume of volcanic material, including subaerial deposits and proximal fallout plus the volcanic edifice (0.2539 ± 0.0069 km^3), constrained through high-resolution surface modeling of the eruption (Civico et al., 2022) and the volatile contents of melt inclusions and matrix glass, we calculated volatile budgets of SO_2 and CO_2 associated with the 2021 eruption using the petrologic approach (Sharma et al., 2004). As melt inclusion volatile compositions are variable through the eruption, and there are uncertainties in other parameters such as erupted volume, melt crystal fraction and lava density, we utilize normal distributions to assess the spread and error associated with all inputs (Figures S3–S6 in Supporting Information S1, see Data Set S1). We use a density of eruptive material value of 2,403 kg/m^3 calculated from the DensityX (Iacovino & Till, 2019) results of this work on matrix glass compositions (2,700 kg/m^3) and the average vesicle modal percent of 11% (Gisbert et al., 2023). We include a density error of 170 kg/m^3 to include the spread of vesicularity values (Gisbert et al., 2023) and DensityX error (Iacovino & Till, 2019). We use a crystal density of 3,010 kg/m^3 calculated from the point counting averages in Table S1 of Ubide et al. (2023). We use a normal distribution, truncated at zero, to obtain a crystal mass fraction of 0.25 ± 0.13, to account for the wide spread of crystallinity estimates within the eruption spanning various grain size fractions (Day et al., 2022; Hornby et al., 2023; Pankhurst et al., 2022; Ubide et al., 2023) (Figure S3 in Supporting Information S1). We utilize a Monte Carlo simulation with 10,000 duplicates to account for uncertainty in vesicularity across all eruptive products. We use an eruption-wide average melt inclusion (3,062 ± 500 ppm) and matrix glass (345 ± 53 ppm) concentrations for SO_2 estimates. A CO_2 budget was calculated using the same methods as for SO_2 with inputs of 12,040 ± 4,553 ppm and 11 ± 7 ppm for melt inclusion and matrix glass concentrations. A HF and HCl budget cannot be calculated as fluorine and chlorine do not degas from the matrix glass in sufficient quantities to be resolvable from analytical noise (Figures 5a and 5c). We use a normal distribution for all measured volatile contents (melt inclusions and matrix glasses) and truncate any negative CO_2 matrix glass values to zero (Figures S4 and S5 in Supporting Information S1).

3. Results

Melt inclusions are hosted within olivine crystals with varying core compositions. To simplify, we discuss these two compositional populations based on the Mg# with one group characterized by lower Mg# (~78–82) present at both the start and end of the eruption, and a higher Mg# population (~83–86) present only in the sample at the end of the eruption (LM0) (see Figure 2 of Dayton et al. (2023)). This spread of olivine Mg# is not unique to the 2021 eruption and has been identified in other eruptive suites over the course of La Palma island growth (e.g., Taburiente volcano, Nikogosian et al., 2002). Melt inclusions trapped within the higher Mg# populations yield olivine-liquid thermometry temperatures of ~1190°C compared to the lower Mg# population with temperatures of ~1160°C (Putirka, 2008, Equation 22). Regardless of host composition, after post-entrapment crystallization (PEC) corrections (details in Supporting Information S1 and Data Set S1), melt inclusions plot along with lava and tephra whole rock as basanites with ~5 wt% total alkalis (Figure 3a). The matrix glass, especially at the start of the eruption (LM6) is significantly more fractionated (Figures 3a and 3b) as expected due to continued magmatic evolution and reflecting the abundance of observed microlites in analyzed tephra fragments and ash particles (cf. Hornby et al., 2023).

PEC-corrected melt inclusions and whole rock lava span MgO contents of 5.5–8.5 wt% with the most mafic inclusions recorded at the end of the eruption (Figure S2 in Supporting Information S1). The FeOt versus MgO variations suggest a liquid line of descent controlled mostly by olivine crystallization up to around ~5.5 wt%

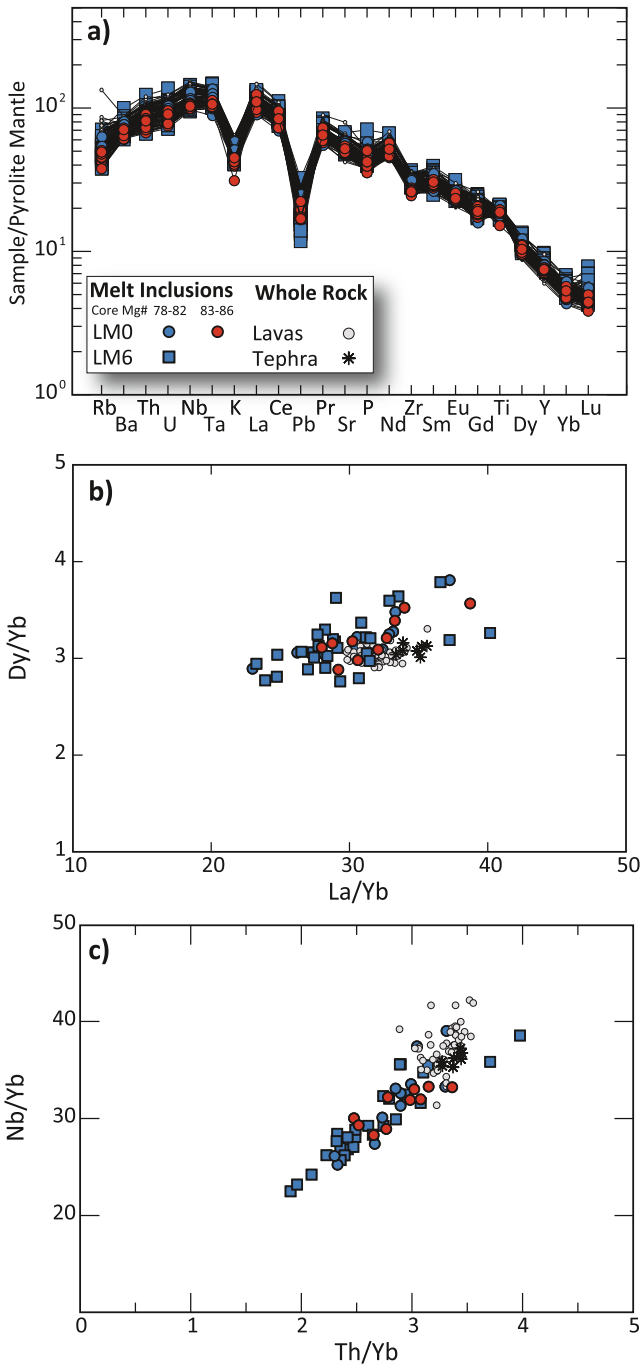

Figure 4. Trace elements from melt inclusions and eruptive materials (tephra and lava) of the Tajogaite eruption. Lava data from Day et al. (2022). (a) Spider diagram normalized to pyrolite mantle (McDonough & Sun, 1995) displaying the compositional homogeneity of eruptive materials. (b) Dy/Yb versus. La/Yb diagram indicating low degree of melt and relative homogeneity among magmas in the garnet peridotite field. (c) Th/Yb versus Nb/Yb discrimination (Pearce & Norry, 1979) diagram identifying all eruptive materials as retaining Oceanic Island Basalt signatures.

MgO, although clinopyroxene and plagioclase have also been observed. Clinopyroxene is also observed as inclusions toward the crystal cores of the lower Mg# olivine population, recording cotectic crystallization during the growth of the most evolved olivine (Figure 2e). Clinopyroxene inclusions are present more infrequently within the lower Mg# rims of the high Mg# olivine crystal population (Figure 2a). The transition between relative fractionated melts recorded at the early stage of the eruption into a more primitive basanite magma (Day et al., 2022; Gonzalez-Garcia et al., 2023; Ubide et al., 2023) is also tracked through melt inclusion CaO/Al_2O_3 (Figure 3b). The most mafic melt inclusions record higher CaO contents, likely reflecting trapping prior to significant clinopyroxene fractional crystallization. Inclusions of magnesiochromite are much more common than pyroxene inclusions and are present within both olivine crystals and melt inclusions (Figure 2).

When our new whole rock tephra data and lava data from previous studies (Day et al., 2022) are compared, the overall trace-element patterns are remarkably similar. The results show depletions in fluid-mobile elements (e.g., K, Pb) and enrichment in high field strength elements (e.g., Nb, Ta, Figure 4a) and light rare earth elements (La/Yb > 10, Figure 4b), which are characteristic of oceanic island basalts (Hofmann, 2007). That said, the range of trace element variations observed within the melt inclusions is larger (e.g., La/Yb 20–40, Nb/Yb 20–40) than what is recorded in the lavas and tephras (La/Yb 30–35, Nb/Yb 35–45) (Figures 4b and 4c) (Maclennan et al., 2003).

Our vanadium-in-olivine estimates of melt inclusion oxygen fugacity of the 2021 eruption span +0.75 to +1.5 FMQ, trending slightly lower than those estimates found by Day et al. (2022) (+1.5 to +2 FMQ) (cf. Canil, 2002). This is likely because the fO2 values of Day et al., 2022 are derived from bulk rock measurements of V, while our V values of in situ melt inclusion measurements from LA-ICP-MS are higher (318 ppm for lava whole rock data vs. 353 ppm V for melt inclusions). Nevertheless, estimates of the V values of olivine from both this work and Day et al. (2022) are very similar, being 5.7 versus 6 ppm, but our fO2 values for the 2021 eruption agree when the uncertainty of the V-in-olivine method is considered (~±0.5 ΔFMQ) (Nicklas et al., 2022). Thus, compared to previous work on the Canary Islands, the 2021 La Palma eruption is slightly less oxidized, but still records an overall oxidized mantle source compared to mid-ocean ridge basalts (Moussallam et al., 2019; Nicklas et al., 2022; Taracsák et al., 2022).

Volatile concentrations of melt inclusions also display a systematic variation between olivine populations with the more evolved melt inclusions population (Mg# 78–82) containing higher concentrations of volatile elements (fluorine, chlorine, sulfur, H_2O) (Figure 5). H_2O concentrations noticeably separate the samples, with inclusions from the start of the eruption (LM6) recording ~1.5–2.5 wt% H_2O and those from the end of the eruption (LM0) showing ~1.0–1.5 wt% H_2O. Despite inclusions from LM0 being hosted in both low Mg# (78–82) and high Mg# (high 83–86) olivine, H_2O contents of melt inclusions from the end of the eruption contain similar H_2O contents regardless of Mg# of the host olivine core (Figures 5a–5d). Sulfur concentrations also divide each sample with early inclusions having between ~3,000 and 4,000 ppm and late inclusions retaining between ~2,000 and 3,500 ppm of sulfur (Figure 5b). However, the volatile divide between low and high Mg# olivine hosted melt inclusions is less noticeable for sulfur and chlorine than it is for fluorine (Figure 5a). Aside from the variations in H_2O, two populations are apparent when fluorine contents are investigated regardless of the sample. Lower Mg# hosted melt inclusions typically contain ~1,400–1,900 ppm

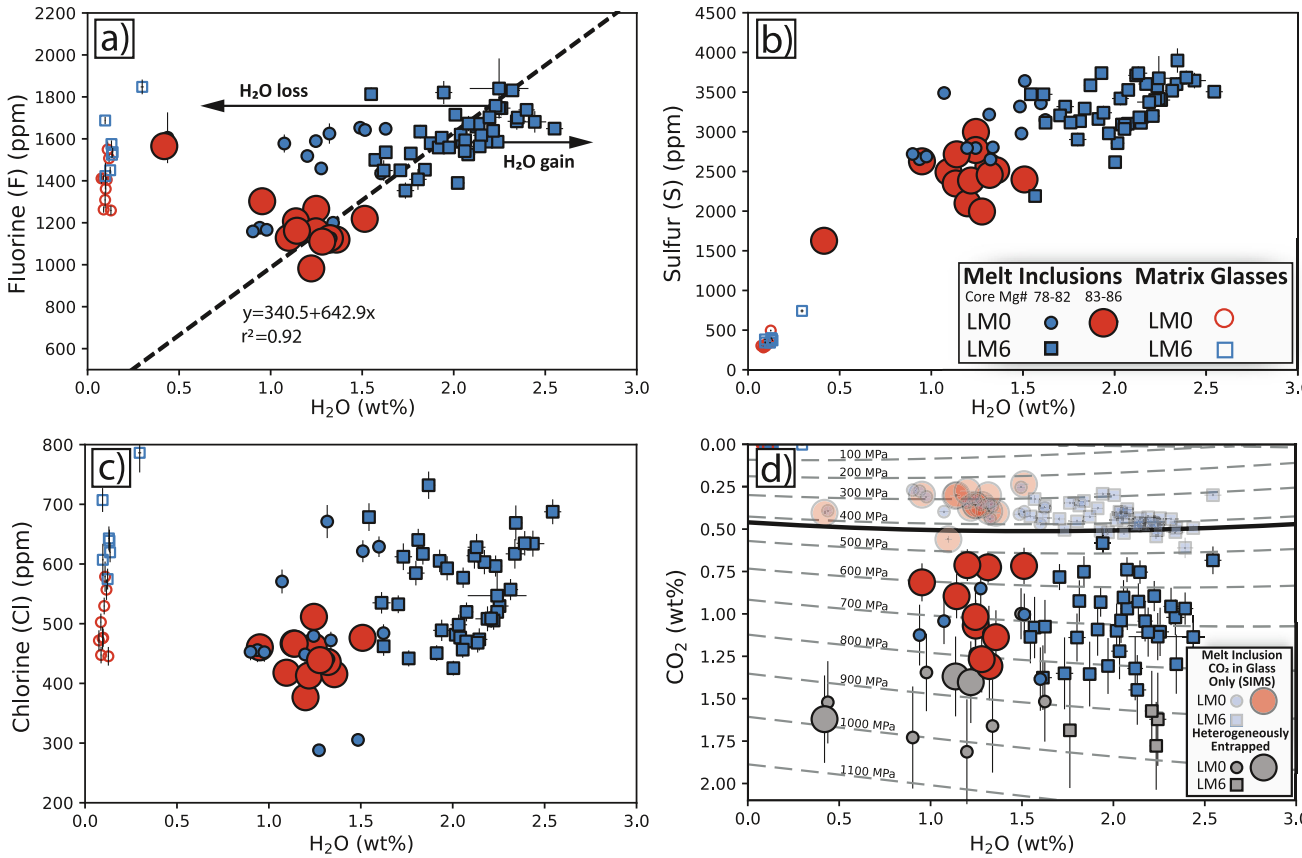

Figure 5. Volatiles (Fluorine, Sulfur, Chlorine, and CO_2 vs. H_2O) of Melt Inclusions and Matrix Glass. (a) Fluorine contents decrease with decreasing H_2O over the course of the eruption. Inclusions in low Mg# olivine from the start of the eruption (LM6) closest to the crystal rims (<30 μm) display some H_2O gain and inclusions trapped in low Mg# crystals erupted toward the end of the eruption (LM0) display the most H_2O loss. Matrix glasses retain a majority of initial fluorine contents. (b) Sulfur decreases with decreasing H_2O in both inclusions and matrix glasses. (c) There is also a decrease of chlorine with H_2O, but the two inclusions with 0.5wt% H_2O have chlorine contents around ~1,100 ppm, indicating later trapping of degassing melt. (d) Melt inclusion total CO_2 (vapor bubble + glass) and melt inclusion glass-only CO_2 (transparent symbols) versus H_2O. Gray symbols are melt inclusions (bubble + glass), which are interpreted as heterogeneously entrapped (Figure 6). Isobars are calculated using Magmasat in VESIcal for a representative composition (PEC-corrected LM6 G3 MI4) with the Moho (black bold line) at 14 km (Ghiorso & Gualda, 2015; Iacovino et al., 2021; Ranero et al., 1995; Tenzer et al., 2013).

fluorine while higher Mg# crystals, all from LM0, contain ~1,000–1,400 ppm fluorine. Interestingly, there are two populations of chlorine contents within the low Mg# hosted melt inclusions (550–750 ppm and <550 ppm), but there is only one population of chlorine contents within the high Mg# population of LM0 (Figure 5c).

CO_2 contents of melt inclusion glasses are slightly higher for sample LM6, resulting in an apparent positive correlation with H_2O (Figure 5d). That said, once the CO_2 within the melt inclusion vapor bubbles are accounted by mass balance, the CO_2 contents in melt inclusions from both samples range from 0.5 to 1.4 wt% CO_2 regardless of Mg# of the host population when inclusions that are potentially heterogeneously co-trapped are excluded (see Section 4.2 and Figures 6 and 7).

4. Discussion

4.1. 2021 La Palma Eruption Volatile Record and Canary Island Volatile Variability

As previously shown, H_2O concentrations in melt inclusions from the same locality, even within single samples, can display considerable variations in H_2O content (Hauri, 2002; Lloyd et al., 2012; Portnyagin et al., 2008). This has been found to depend on the grain size selected for inclusion analysis due to rapid H_2O diffusivity upon clast cooling, and several studies have employed experimental techniques to reverse and constrain these changes (Bucholz et al., 2013; Gaetani et al., 2012; Portnyagin et al., 2008; Rasmussen et al., 2020; Wallace et al., 2015). To avoid these complications, we selected olivine crystals coated only with a thin veneer of glass sieved from a

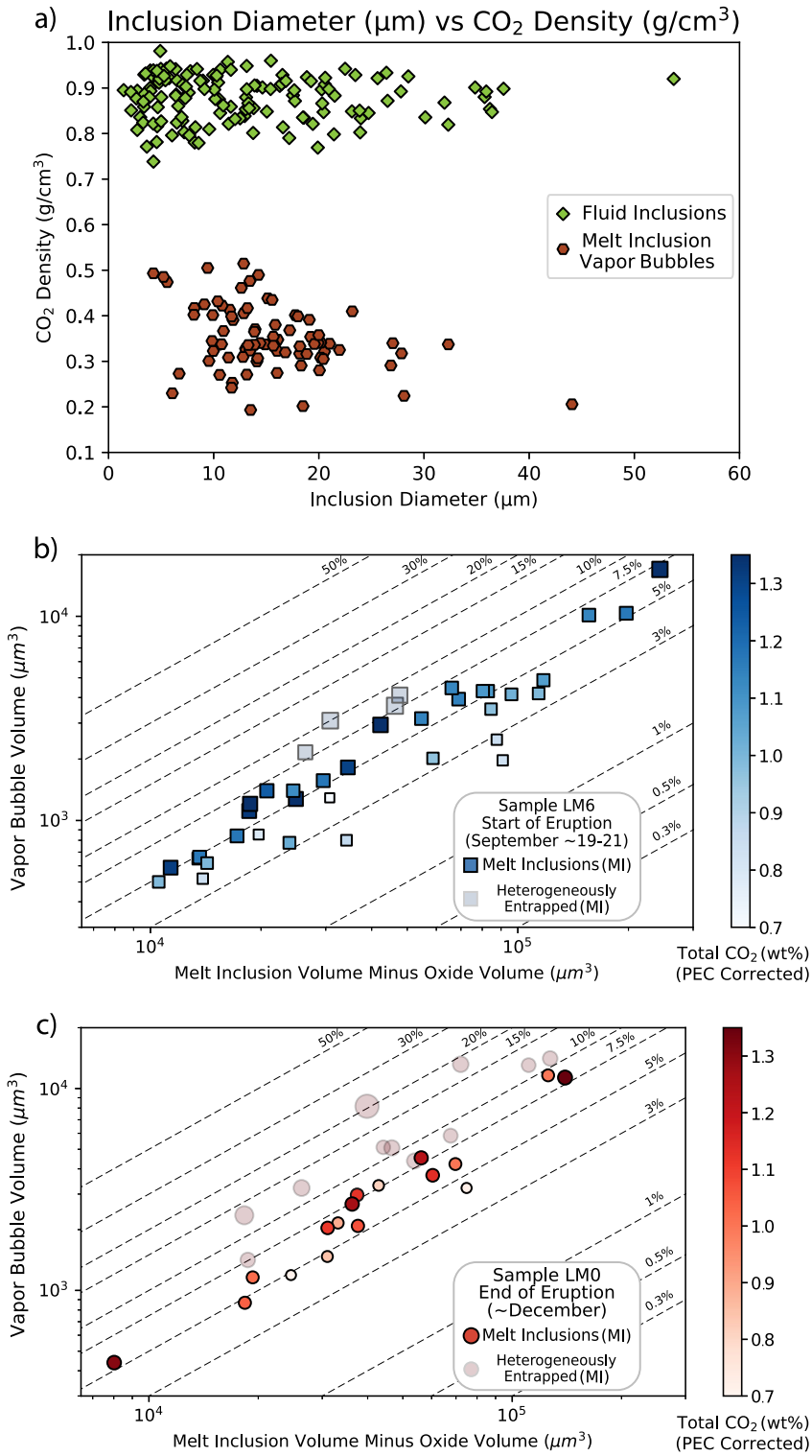

Figure 6. Evaluation of CO_2 density, melt inclusion volumes, and heterogeneous entrapment. (a) CO_2 density (g/cm^3) of melt inclusion vapor bubbles and non-decrepitated fluid inclusions from this work and Dayton et al. (2023) versus inclusion diameter (μm). (b) Melt inclusion volume versus bubble volume for sample LM6 (start of the eruption) sized and colored by total PEC corrected CO_2. The inclusions circled in gray are interpreted to be heterogeneously entrapped. (c) Melt inclusion volume versus bubble volume for sample LM0 (end of the eruption) sized and colored by total PEC corrected CO_2. The inclusions circled in gray are interpreted to be heterogeneously entrapped.

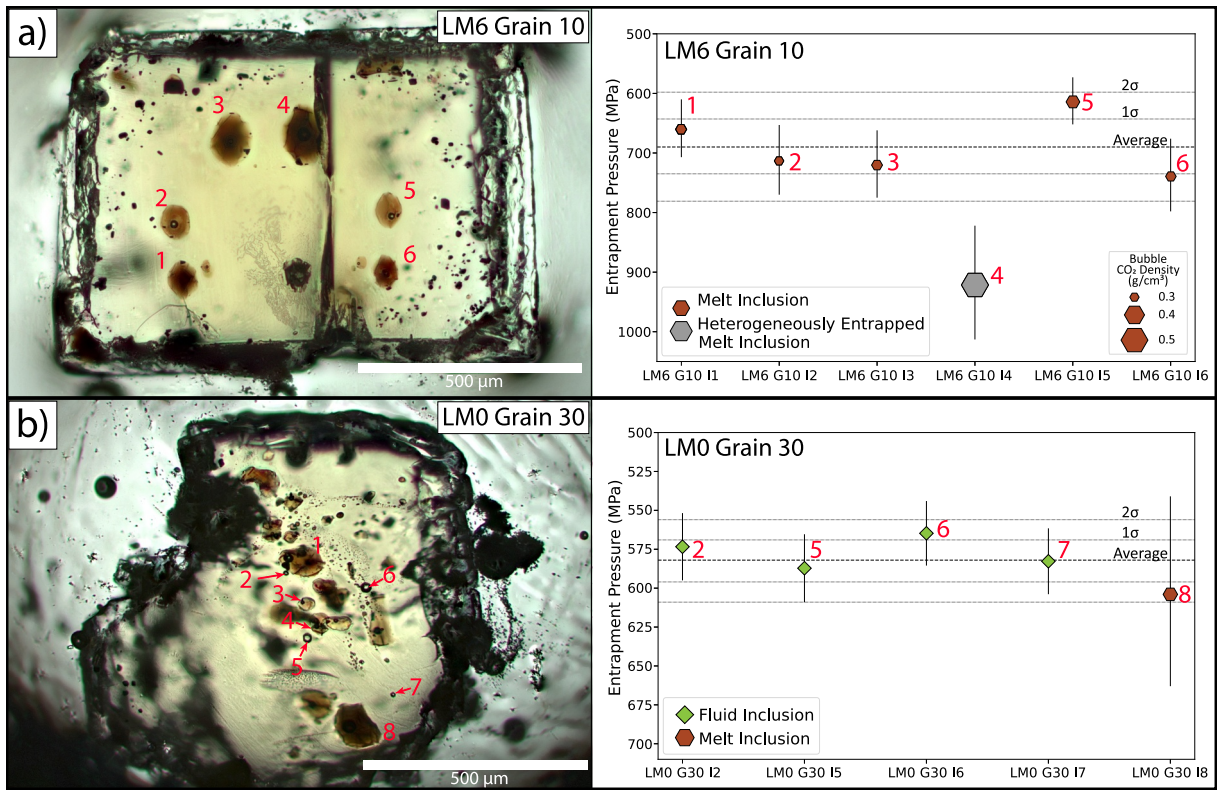

Figure 7. Multiple Inclusions in Single Crystals (note: these are focus stacked images to allow inclusions at different depths to be visible within a single image) (a) LM6 Grain 10 contains six analyzed melt inclusions with all inclusions preserving approximately the same H_2O contents (~2.2–2.3 wt%). Five of the six inclusions retain saturation pressures of ~700 MPa, or ~24.5 km and a CO_2 vapor bubble densities of 0.33–0.35 g/cm^3. Inclusion four is heterogeneously entrapped recording a saturation pressure of ~900 MPa, ~31.6 km and a CO_2 vapor bubble density 0.47 g/cm^3. (b) LM0 Grain 30 with four fluid inclusions and one melt inclusion. All inclusions retain entrapment pressures within error.

fine grain size fraction of 0.5–2 mm to ensure rapid quenching, following the best practice recommendations of Lloyd et al. (2012).

We find that melt inclusions in lower Mg# (78–82) crystals erupted during the opening (sample LM6) of the eruption record the highest H_2O content (up to 2.5 wt%). To properly evaluate the diffusive loss or gain of H_2O during ascent, we plotted our H_2O contents against other volatiles (e.g., fluorine, chlorine, sulfur) and measured the distance from the melt inclusion to the crystal edge along the a-axis, in which H_2O diffuses the fastest (Barth et al., 2019; Ferriss et al., 2018; Le Voyer et al., 2014). We did not find major differences in melt inclusion volume or distance to crystal edge in either sample. As fluorine did not degas from the co-erupted matrix glasses (Figure 5a), we assume that fluorine did not diffuse from melt inclusions as concentrations remained in equilibrium with their carrier melt (Bucholz et al., 2013; Le Voyer et al., 2014; Portnyagin et al., 2008), but note the lack of consensus on the behavior of fluorine in olivine (Koleszar et al., 2009). When H_2O is plotted against fluorine, we find minimal H_2O loss in inclusions at the start of the eruption (LM6), with a few exceptions. We notice that inclusions very close to the edge of crystals along the a-axis (<30 µm) likely gained some H_2O (Figure 5a) based on multiple inclusion measurements in single crystals as those closest to the grain edge have slightly elevated H_2O contents (~0.2 wt%) (e.g., LM6 Grain 2). We interpret this slight H_2O gain as melt inclusion rehydration and incomplete re-equilibration during magma ascent as olivine crystals from LM6 encountered the evolved, hydrous, amphibole-bearing tephrite melt (see LM6 matrix glass composition, Figure 3) that was emitted during the first days of the eruption (Day et al., 2022; Pankhurst et al., 2022; Ubide et al., 2023).

These low Mg# crystals were the primary crystal cargo during the start of the eruption (sample LM6) but were also sampled together with a lower H_2O and higher Mg# (83–86) population toward the end of the eruption (both within sample LM0) (Figure 5). As mentioned, the melt inclusions from the end of the eruption are hosted in two populations of olivine, but regardless of Mg#, all the late erupted crystals contain melt inclusions which record

concentrations of ~1.0–1.5 wt% H_2O. Given the lower fluorine, sulfur, and chlorine concentrations of the melt inclusions within the high Mg# olivine population (red circles, Figure 5), we interpret these inclusions as initially containing lower water concentrations, rather than being fully controlled by water loss. We identify the lower Mg# population that erupted at the end of the eruption (blue circles, Figure 5) as genetically related to the initial lower Mg# crystal cargo sampled at the beginning of the eruption in sample LM6 (blue squares). The lower H_2O in the lower Mg# population from the end of the eruption is likely controlled by diffusive hydrogen loss, which occurs on the scale of hours in olivine within the Mg# range (78–82) (Barth et al., 2019). We explain this relationship among the lower Mg# olivine population seen at the end of the eruption by having resided in the volcanic plumbing system for a longer time and thus interacting with new, more H_2O poor magma replenishments within the plumbing system. The influx of the drier, more primitive magma (recorded by melt inclusions with high CaO/Al_2O_3 in the higher Mg# olivine crystals) (Figure 3) drove diffusive re-equilibration of the H_2O contents of the lower Mg# hosted inclusions that erupted at the end of the eruption.

Overall, we see positive correlations between H_2O and fluorine, chlorine, and sulfur (Figures 5a–5c) in these melt inclusions, with lower Mg# crystals containing inclusions higher in fluorine, chlorine, and sulfur regardless of sample. Generally, incompatible volatile elements are higher in the lower Mg# olivine populations, suggesting volatile increase connected with fractional crystallization. Our analyzed melt inclusions do not record evidence of sulfur saturation, identified by the presence of sulfide blebs (Hartley et al., 2017), except in two heterogeneously entrapped inclusions with anomalously low H_2O (~0.5 wt%) and high chlorine contents (~1,000 ppm) (Figure 5; LM0 Grain 1 Inclusion 1 and LM0 Grain 23 Inclusion 1; see Supporting Information S1 and Data Set S1). Observed sulfide and ubiquitous magnesiochromite inclusions are identified through Raman spectroscopy (Lafuente et al., 2015).

Our fluorine contents of melt inclusions from the 2021 eruption align with those from the 1949 eruption (Duraznero vent), Barranco Fagundo deposits (of the main Taburiente shield volcano), and other Holocene cones on La Palma (Kirstein et al., 2023; Walowski et al., 2019), but we have found higher H_2O (up to 2.5 wt%) agreeing with phase equilibrium experiments (Fabbrizio et al., 2023). Compared to the most volatile rich inclusions of the El Hierro 2011–2012 eruption, which contain over 3 wt% H_2O, 5,000 ppm sulfur, and 2,000 ppm fluorine (Longpré et al., 2017) and other El Hierro inclusions (Taracsák et al., 2019), the inclusions of the 2021 La Palma eruption are slightly less volatile rich. Tenerife melt inclusions from 1705 Volcán de Fasnia (TF-16-08) and Montaña Bilma (TF-16-09A) eruptions (DeVitre, Gazel, et al., 2023) also contain very similar H_2O, CO_2 (in melt inclusion glass), fluorine, chlorine, and sulfur contents as the 2021 La Palma eruption in similar olivine host populations, indicating that similar volatile systematics may apply on an inter-island scale.

We found half the amount of chlorine in our samples for the 2021 eruption (~300–800 ppm, with later trapped inclusion containing ~1,100 ppm) versus 600–1,900 ppm found in previous studies of melt inclusions from earlier eruptions on La Palma (Kirstein et al., 2023; Walowski et al., 2019). An overestimate in chlorine concentrations by the SIMS at Edinburgh Ion Microprobe Facility (EIMF) was noted by Taracsák et al. (2019) when analyzing melt inclusions from El Hierro, which may explain the chlorine discrepancy between melt inclusion populations from older La Palma eruptions as SIMS data was collected at EIMF (Kirstein et al., 2023; Walowski et al., 2019). To evaluate this discrepancy, the chlorine contents of our melt inclusions were also measured using EPMA, with results in agreement with SIMS data from WHOI (Supporting Information S1 and Data Set S1). Inclusions from the 2011–2012 eruption of El Hierro (Longpre et al., 2017), also measured at WHOI, record chlorine contents (~600–1,300 ppm) higher than those from La Palma but lower than those measured at EIMF (150–1,700 ppm; Taracsák et al., 2019). Chlorine contents are especially important when comparing F/Cl ratios, with recent work (Hartley et al., 2022) finding average F/Cl ratios of melt inclusions from the 2021 eruption of ~1.9, while we find average F/Cl of ~3 in our melt inclusions.

Despite lower fluorine, chlorine, and sulfur when compared to previous La Palma and El Hierro eruptions, the glass phase of the 2021 melt inclusions contains some of the highest dissolved CO_2 of the Canary Islands. Maximum CO_2 contents reach up to 6,000 ppm versus 4,000 ppm in the 1949 eruption products and Barranco Fagundo deposits (Walowski et al., 2019) and ~3,500 ppm in El Hierro eruption products (Longpré et al., 2017; Taracsák et al., 2019). Maximum CO_2 contents of melt inclusion glasses may also be due to compositional variations among eruptions, resulting in differences in CO_2 solubility as well as differences in CO_2 partition within vapor bubbles (Moore et al., 2015; Shishkina et al., 2014).

4.2. 2021 La Palma Eruption Volatile Record and Canary Island Volatile Variability

While a lack of vapor bubble data from previous La Palma eruptions hinders comparisons between eruptions, variations in total CO_2 contents in our combined vapor bubble and glass data can be compared to identify changes within the 2021 eruption. Almost all selected melt inclusions from both sample sets had CO_2 detectable by Raman spectroscopy in vapor bubbles with CO_2 densities ranging from 0.19 to 0.51 g/cm^3. On the other hand, non-decrepitated fluid inclusions retained CO_2 densities between ∼0.74–0.98 g/cm^3 (Figure 6a) (Dayton et al., 2023). Specifically, LM0 Grain 2 Inclusion 2 (pictured in Figures 2a and 2b) had no detectable CO_2 in the vapor bubble. Other inclusions with a similar morphology (rounded, smooth, and unfaceted) have also been found to not contain CO_2 in the vapor bubble, as these vapor bubbles formed during quenching and CO_2 did not have time to diffuse into the vapor bubble (cf. Maclennan, 2017; Wieser et al., 2021). This shallower, later-trapped inclusion (LM0 Grain 2 Inclusion 2, 15.8 ± 0.4 km) was large enough to allow for SIMS data collection and comparison with a more primitive, deeper-trapped inclusion (LM0 Grain 2 Inclusion 1, 19 ± 1.5 km) trapped within the same crystal (Figures 2a and 2b).

As evident by inclusions with large bubble-volume percent and the presence of fluid inclusions in phenocrysts (Dayton et al., 2023), heterogenous entrapment of exsolved CO_2 fluid occurs in some melt inclusions (e.g., Steele-MacInnis et al., 2017). From our selected melt inclusions, vapor bubbles occupied between ∼3%–20% of the melt inclusion volume (minus co-trapped oxide volumes; Figures 6b and 6c). We find that inclusions with a bubble-volume percent above 7.5 ± 1.5 for LM6 and 10 ± 1.5 for LM0 (plotted with opaque symbols on Figures 6b and 6c) and total reconstructed (vapor bubble plus glass) PEC-corrected CO_2 above ∼1.4 wt% indicate heterogenous entrapment. We note that vapor-bubble percent alone cannot identify heterogenous entrapment and melt inclusions must be measured in all three dimensions to obtain the best estimates of vapor-bubble-volume percent (DeVitre, Gazel, et al., 2023; Mironov et al., 2020). If the third dimensions of these melt inclusions were assumed from measurements of the exposed two dimensions, vapor bubble percents of these inclusions would be significantly lower with an average of 2.3% for this sample set. Whereas when the shortest, third dimension of these melt inclusions are measured, in this case with Raman spectroscopy (see Data Set S1), this sample set has an average vapor bubble percent of 6.5%.

In addition to anomalously high reconstructed PEC-corrected CO_2 contents (bubble plus glass), saturation pressures, and bubble volume percent, we find that inclusions with more than ∼75% CO_2 in the vapor bubble for LM0 and 70% in the vapor bubble for LM6 also indicate heterogeneously entrapped melt inclusions in these samples. We find that vapor bubbles of inclusions within the dehydrated, low Mg# hosted melt inclusions of LM0 erupted at the end of the eruption (Figure 5) contain the highest percentage of CO_2. We note that heterogeneous entrapment is more common in crystals erupted during the end of the eruption within LM0 (Figure 6b), potentially indicating more exsolved CO_2 fluid as the eruption progressed.

Heterogeneous entrapment of melt inclusions can be further identified by analyzing multiple inclusions within the same inclusion assemblage in the same crystal. LM6 Grain 10 contains six melt inclusions analyzed with all analytical techniques (Raman, SIMS, EPMA, LA-ICP-MS) (Figure 7a). Inclusion 4 is heterogeneously entrapped and records a spurious saturation pressure of 900 MPa, while the five other melt inclusions record pressures of ∼700 MPa when total CO_2 contents are reconstructed (bubble plus glass). Upon further investigation, LM6 Grain 10 Inclusion 4 has a bubble volume percent of 7% and a CO_2 density of 0.47 g/cm^3, while the other five inclusions have bubble volume percent between 3.4% and 5.7% and CO_2 densities between 0.33 and 0.35 g/cm^3.

Unfortunately, identifying heterogenous melt inclusions from previous studies is difficult without accurate measurements of melt inclusions in all three dimensions. When inclusions from the La Palma 2021 eruption are compared to those from other studies of Canary Island melt inclusions that reported CO_2 in melt inclusion vapor bubbles, the La Palma 2021 eruption melt inclusions contains more CO_2 (up to 1.4 wt%) than those of El Hierro (up to ∼1.3 wt%, Taracsák et al., 2019) and Tenerife (up to 1.3 wt%, DeVitre, Gazel, et al., 2023), though these highest estimates of other studies may be inaccurate as heterogenous entrapped inclusions cannot be identified. Nevertheless, this indicates that a deeper magma storage reservoir fed the 2021 La Palma eruption as recorded through higher CO_2 contents.

4.3. Comparing Melt and Fluid Inclusions in Single Crystals

To investigate if melt and fluid inclusions record equivalent pressures within the 2021 magma reservoir, we identified grains which contained both melt and fluid inclusions within a single crystal to directly compare preserved pressures from both inclusion types in grains with similar histories (Figure 7b). Overall, grains containing both melt and fluid inclusions are rare. Even if both types of inclusions are within the same crystal, inclusions must be suitable for comparisons. Fluid inclusions must not be decrepitated, so they retain their original trapping pressures (unlike the decrepitated fluid inclusion in Figure 7a) (Campione, 2018; Campione et al., 2015; Wanamaker et al., 1990) and melt inclusions must not be heterogeneously entrapped (Figures 2c and 7a) to preserve their true trapping pressure (Steele-MacInnis et al., 2017). To complicate this comparison further, we find that melt inclusions within grains that also have fluid inclusions are commonly heterogeneously entrapped as crystal growth may occur near areas with exsolved CO_2 fluid (ex. LM0 Grain 25 Inclusion 2) (Figure 2c).

Despite fluid and melt inclusions being trapped within the same grain, careful consideration must also be taken to ensure the inclusions are petrogenetically related and they belong to the same fluid-inclusion assemblage (FIA) (Goldstein & Reynolds, 1994) or in this case, inclusion assemblage. This is displayed in LM6 Grain 28 (Figure 2d, note these images are focus-stacked to allow photographing of inclusions at different depth within the same crystal in a single image), which contains multiple inclusions assemblages. Melt inclusions 3 and 4 belong to the same assemblage recording pressures of 735–756 ± 60 MPa (25.5–26 ± 2 km). While a ∼3 μm fluid inclusion trapped within a different inclusion assemblage (inclusion 5; Figure 2d), cross-cutting below the inclusion assemblage that contains inclusions 3 and 4 within this same crystal records a pressure of 590 ± 22 MPa (17.6 ± 0.7 km).

On the rare occasion that both suitable melt and fluid inclusions are trapped within the same inclusion assemblage (Goldstein & Reynolds, 1994), a comparison between inclusion types can be evaluated. In LM0 Grain 30 (Figure 7b), both fluid inclusions (inclusions 2, 5, 6, and 7) and a melt inclusion (inclusion 8) are trapped within a single inclusion assemblage and record pressure between 560 and 600 MPa (∼20 km). This indicates that inclusions trapped within the same assemblage may record similar pressures and single crystals can record multiple events at different depths by analyzing multiple assemblages and different inclusion types. By analyzing both melt and fluid inclusions within crystals, we are also allowed a glimpse into a single crystal's journey through a magma chamber, identifying magmatic processes at different depths.

4.4. Reconstructing Magmatic Plumbing System

Overall, melt inclusions retain slightly higher pressures than fluid inclusions, but average depths and pressures are within error of each other (839 ± 75 MPa or 29 ± 2.5 km for the deepest melt inclusion vs. 780 ± 27 MPa or 27 ± 0.9 km for the deepest fluid inclusion; Dayton et al., 2023). This may be due to the higher uncertainty of saturation pressure calculations using a solubility model for melt inclusions or as the fluid inclusion densities of Dayton et al. (2023) assume a pure CO_2 fluid using the equation of state of Span and Wagner (1996) (Figure 8). As the quantity of H_2O in CO_2 fluid inclusions could not be directly determined, we re-calculate fluid-inclusion pressures and depths using the molar fraction of H_2O (XH2O) values of melt inclusions with MagmaSat (Ghiorso & Gualda, 2015; Iacovino et al., 2021). We use average values of XH2O of 0.15 for LM6 and 0.05 for LM0 and utilize the mixed CO_2-H_2O equation of state of Duan and Zhang (2006) republished by Yoshimura (2023) and implemented into DiadFit (Wieser & DeVitre, 2023). If XH2O of melt inclusions is applied to fluid inclusions within the same samples, we find that fluid inclusions for LM6 record entrapment depths 6 km (186 MPa) deeper and those from LM0 would be placed 2 km (54 Mpa) deeper (see Supporting Information S1 and Data Set S1). Despite these changes in entrapment pressure, melt and fluid inclusions still align within error. We note that as more work is needed on the diffusion of H_2O out of CO_2 fluid inclusions at magmatic temperatures, we discuss the fluid-inclusion data as published in Dayton et al. (2023). There is a lack of fluid inclusions retaining pressures from the 2021 eruption above 780 ± 27 MPa (27 ± 0.89 km), which may indicate that CO_2 did not significantly exsolve deeper than ∼27 km, corresponding with the deepest depths of earthquake epicenters recorded during the 2021 eruption (D'Auria et al., 2022; Dayton et al., 2023).

In addition to intact fluid inclusions, decrepitated fluid inclusions were analyzed. Inclusions with any optically identifiable indications of decrepitation (Campione, 2018; Campione et al., 2015; Wanamaker et al., 1990) were excluded from Dayton et al. (2023) but are now evaluated further (Figure 8). Some fluid inclusions with optically identifiable features of decrepitation still retain densities of ∼0.7 g/cm^3, indicating decrepitation and equilibration

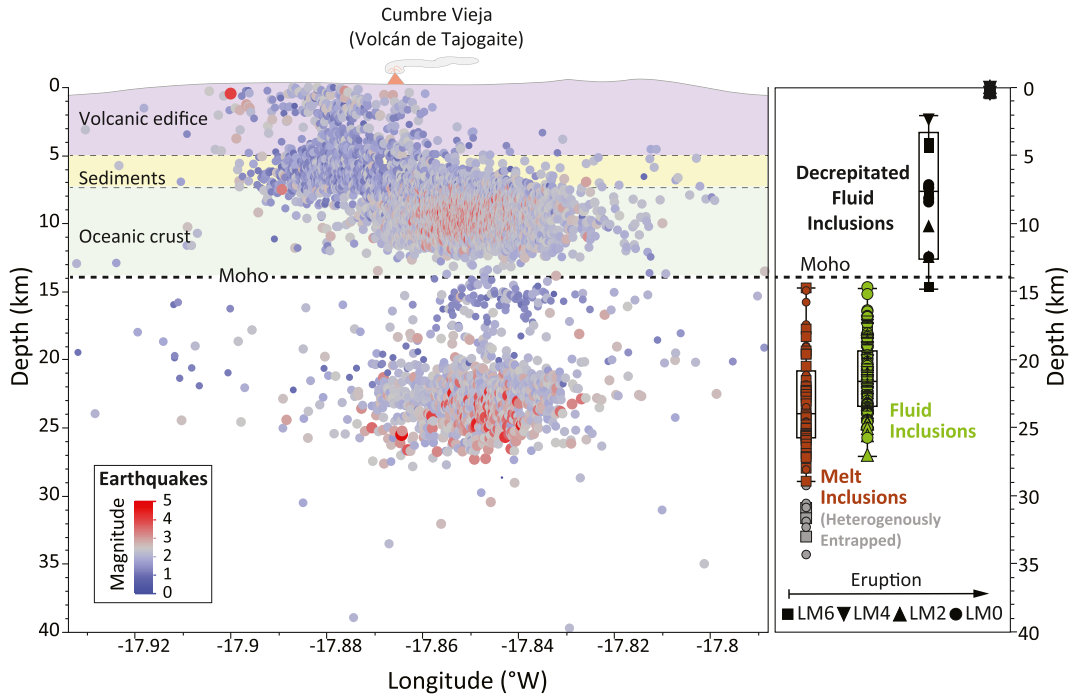

Figure 8. Cross-section of the magmatic plumbing system under Cumbre Vieja. Deep and shallow earthquakes (D'Auria et al., 2022) indicate two main reservoirs. Fluid inclusions (Dayton et al., 2023; this work), and melt inclusions plot together below the Moho at 14 km (Ranero et al., 1995; Tenzer et al., 2013). Heterogeneously entrapped melt inclusions are plotted in gray. Decrepitated fluid inclusions in the olivine plot in two groups, one between 2 and 14 km aligned with the shallower earthquakes and upper magma chamber within the crust, and another population recorded depths of ~0.3 km, which we interpret as representing decrepitation upon final magma ascent.

within the deep mantle chamber prior to further ascent. Generally, decrepitated fluid inclusions retain two groups of separate pressure ranges in addition to the deep mantle magma reservoir.

One group of decrepitated fluid inclusions retained CO_2 densities between 0.2 and 0.6 g/cm^3, corresponding to pressures between 60 and 340 MPa (2.5–12.5 km) and aligned with the upper earthquake swarm within the crust (Figure 8) (D'Auria et al., 2022; Del Fresno et al., 2023). The second group of decrepitated fluid inclusions displayed ultra-low densities between 0.001 and 0.05 g/cm^3, with the lowest densities right at the detection limit of our Raman spectroscopy method (DeVitre et al., 2021). These ultra-low-density inclusions indicate fluid inclusion decrepitation upon ascent and preserve pressures of under 10 MPa (or less than 0.5 km). The preservation of CO_2 within decrepitated fluid inclusions indicates rapid olivine fracture healing following loss of initial trapping pressure (Wanamaker et al., 1990). This allows decrepitated inclusions to record additional, shallower, magma storage depths as they rapidly re-equilibrate to their evolving storage conditions.

4.5. Geochemical Evolution of the 2021 La Palma Eruption

Despite relatively uniform compositions, subtle geochemical changes in eruptive products can serve as indicators of magmatic processes at depth. While in a TAS diagram (Figure 3a) (Le Bas et al., 1986) erupted products (excluding matrix glasses) generally plot together as tephrites/basanites, changes in the magma supply are apparent in lavas and melt inclusions when investigating CaO/Al_2O_3 versus SiO_2 for the duration of the eruption (Figure 3b). Though whole rock composition of the 2021 lavas identifies a generally homogenous mantle source with input of a young HIMU recycled oceanic lithosphere and relatively uniform degree of partial melting (2.5%–3%) (Day et al., 2022), variations in Os isotopes identify fractional crystallization or even a degree of crustal contamination, specifically in eruptive products from the first 20 days of eruption. This differentiation of early erupted magma results in the evolved compositions of the matrix glasses from the first days of the eruption (LM6) and the early eruption of amphibole. In addition, this is in line with the slight re-hydration of melt inclusions within olivine erupted during the first days of the eruption (cf. Day et al., 2022; Ubide et al., 2023) (Figures 5a and

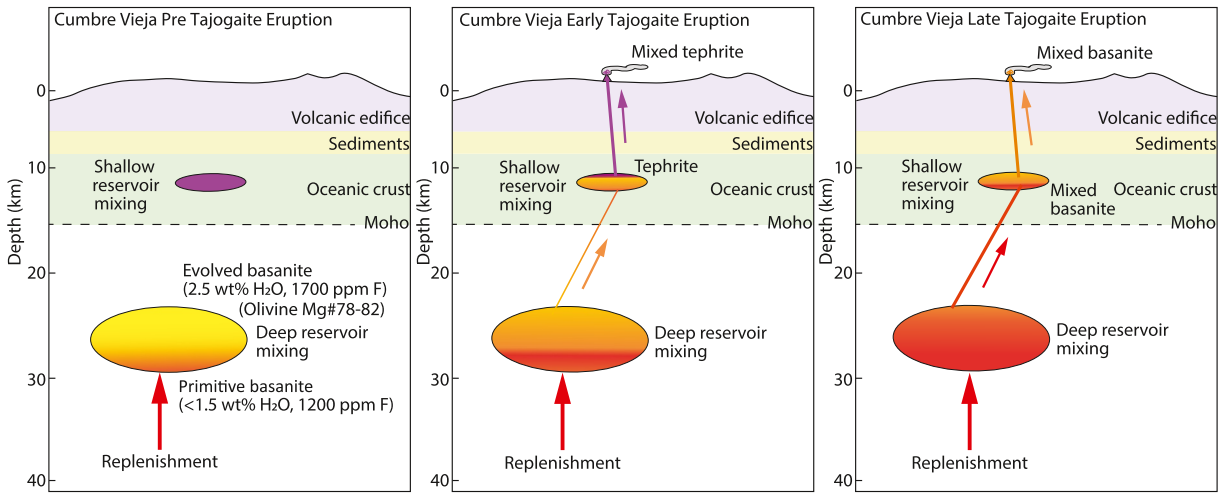

Figure 9. Schematic diagram of the Tajogaite eruption based on the results of this study. Prior to eruption, magma fractionates within both the shallow and deep reservoirs, creating the evolved tephrites and basanites. Following magma replenishment, this evolved composition, along with more evolved low Mg# olivine phenocrysts retaining the more volatile enriched melt inclusions, was cleared out of the magma chamber. Following replenishment, the primitive lower volatile-rich composition begins to dominate the eruption, entraining the more primitive higher Mg# olivine phenocrysts and melt inclusions.

9). Notably, melt inclusions within the low Mg# olivine population also record this pre-eruptive fractionation through lower CaO/Al_2O_3 ratios (Figure 3b) and inclusions of clinopyroxene (Figures 2a and 2e).

In situ analysis uncovers a more detailed picture of distinct melt batches exhumed during the eruption. In situ Sr isotope data traces two distinct magma batches, and identifies a colder, more radiogenic, evolved crystal mush at the beginning of the eruption (high $^{87}Sr/^{86}Sr$ in andesine) and a less radiogenic, mafic melt (lower $^{87}Sr/^{86}Sr$ in labradorite microcrysts) (Ubide et al., 2023). Melt inclusion compositions along with isotope studies (Day et al., 2022; Sandoval-Velasquez et al., 2023; Ubide et al., 2023) identify the exhumation of this new batch of less fractionated magma in November 2021 (Day et al., 2022; Ubide et al., 2023) recorded by the change in CaO/Al_2O_3 versus SiO_2 of lava around day 50 of the eruption and is sampled by melt inclusions within the high Mg# olivine population in LM0 (Figure 3b).

Our melt inclusion data further constrains this process to specific depths, and although trace element variation between samples is small, volatile contents within melt inclusions trace fractional crystallization and pulses of hotter primitive magma replenishment (Figures 5 and 9). Melt inclusions that record this fractionation processes with elevated H_2O, sulfur, chlorine, and fluorine (hosted within low-Mg# olivine) record pressures spanning the entire deep magma reservoir (17.6 ± 1.3–29 ± 2.5 km), indicating that fractionation occurs throughout the entire deep chamber system. As the eruption began to be overtaken by the more primitive magma supply (Figure 9), we find that these lower-Mg# crystals containing inclusions of the early appearing derivative magmas become less frequent as this presumably older crystal mush is evacuated from the deep chamber and becomes entrained with the higher-Mg# crystals recording the emplacement of more primitive melt. Our analyzed melt inclusions recording this primitive melt record pressures between 14.9 ± 1.4 and 28.1 ± 2.7 km and align with fluid-inclusion pressures from the same sample (15–27 km) (Dayton et al., 2023), tracing this primitive magma through the entire deep magma chamber. Melt inclusions hosted within more evolved crystal cargoes that crystallized from a more H_2O-rich evolved magma likely underwent diffusive re-equilibration with the more primitive, H_2O-poor replenishing magma, resulting in the significantly lower H_2O contents of the melt inclusions in the lower Mg# olivine of LM0 (blue circles, Figure 5) compared with the same population at the beginning of the eruption within LM6 (blue squares, Figure 5). This natural dehydration has implications for melt-inclusion studies which characterize the volatile contents of an eruption using a single sample, as our results show that melt inclusion H_2O contents can vary significantly between different samples (Bucholz et al., 2013; Gaetani et al., 2012; Portnyagin et al., 2008).

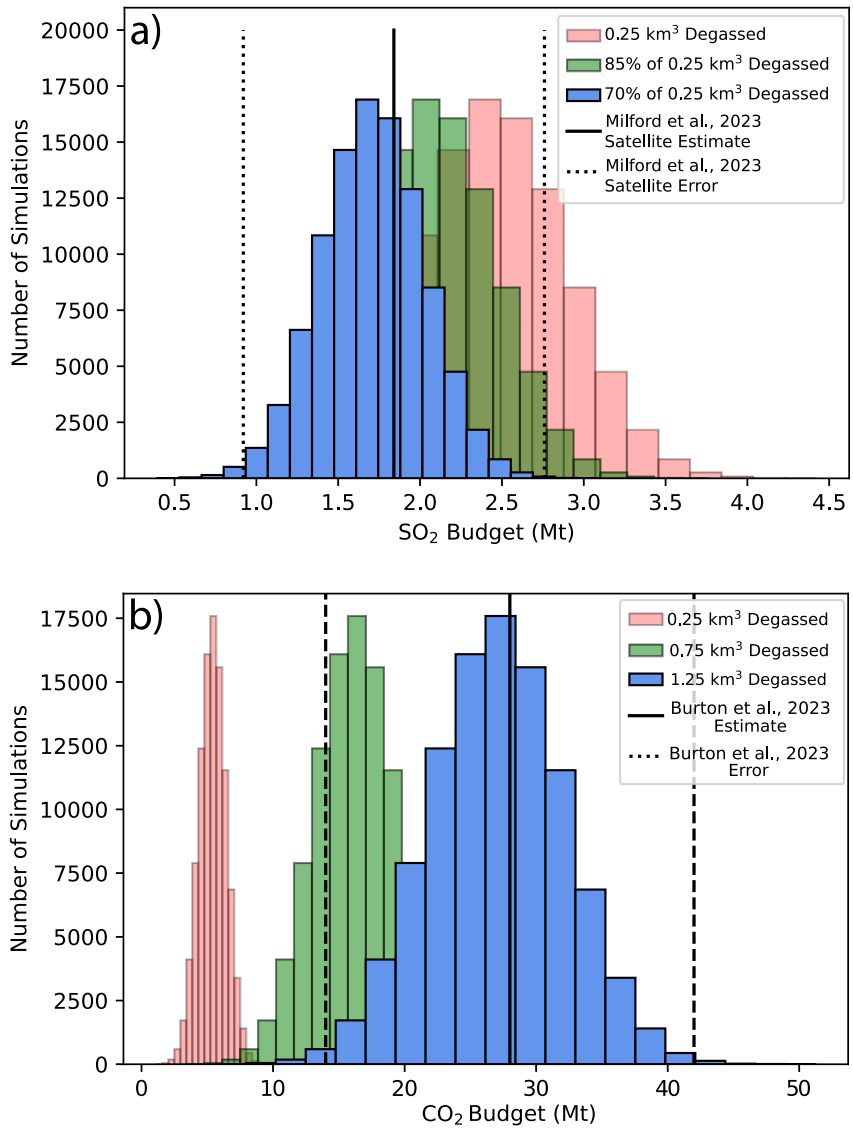

Figure 10. Atmospheric emissions of (a) SO_2 calculated for the Tajogaite eruption using the petrographic method of Sharma et al. (2004). Errors in input parameters were propagated using Monte Carlo simulations and budgets are reported for three scenarios: full degassing (melt inclusion-matrix glass), 85% degassing, and 70% degassing of erupted material using the 0.25 km^3 volume estimates of Civico et al. (2022). Reported satellite data and error on SO_2 emissions are from Milford et al. (2023) and Valade et al. (2019). (b) CO_2 budget calculated using the same methods as for SO_2, but for scenarios where for 0.25 km^3 (actual volume; Civico et al., 2022), 0.75 km^3, and 1.25 km^3 of magma degassed. Black lines indicate the CO_2 estimates and error of Burton et al. (2023).

4.6. Volatile Budgets of the 2121 La Palma Eruption

Our Monte Carlo simulations suggest that over the span of the 2021 eruption, 2.4 ± 0.4 Mt of SO_2 would have been emitted from the degassing (determined from the difference between melt inclusion and matrix glass composition) of 0.25 km^3 of eruptive materials. This is higher, but within error of the 1.84 ± 0.92 Mt estimates from satellite-constrained emissions (Milford et al., 2023; Valade et al., 2019) (Figure 10a). This discrepancy can be reconciled in a number of ways. First, it is possible that satellites underestimate the emission rate if the cloud fraction is high and plume altitude is low (Esse et al., 2023). Second, it may be that some proportion of the erupted lava did not experience as much degassing as the matrix glasses measured here (e.g., lava transported in closed tubes). We address this scenario by performing the same calculation assuming that the average amount of degassing of 0.25 km^3 of erupted material was 85% and 70%. If only 70% of the accounted for erupted volume is

degassed, SO_2 emissions from the petrographic method (2.0 ± 0.4 Mt) and satellite estimates of 1.84 ± 0.92 Mt (Milford et al., 2023) more closely align (Figure 10a). Third, there are also other sources of uncertainty that may resolve offsets between satellite and petrological methods. The presence of fumarolic deposits containing native sulfur and sulfates (as well as carbonates, fluorides, and chlorides, Campeny et al., 2023; Martínez-Martínez et al., 2023), and the formation of sulfate crystals on fine volcanic ash (Hornby et al., 2023) during the 2021 indicate that some amount of emitted sulfur was sequestered prior to detection by satellites. Using the 100% degassing of 0.25 km^3 of the eruptive volume scenario, it is noteworthy that the La Palma 2021 eruption's emission of 2.4 ± 0.4 Mt of SO_2 pales in comparison to the 2018 lower East Rift Zone eruption of Kīlauea which emitted ∼10 Mt of SO_2 (Kern et al., 2020). Despite the higher sulfur concentrations of the La Palma melt inclusions (3,062 ± 500 ppm) and matrix glasses (345 ± 53 ppm) compared to Kīlauea 2018 melt inclusions (400–900 ppm) and matrix glasses (100–900 ppm) (Lerner et al., 2021), the Kīlauea 2018 eruptive volume (0.9–1.4 km^3 DRE) was significantly larger than the 2021 La Palma eruption (0.21–0.24 km^3 DRE) (Dietterich et al., 2021). For the La Palma 2021 eruption to release as much SO_2 as the Kīlauea 2018 eruption, only 0.84–0.96 km^3 DRE would be needed to emit 9.7 ± 1.8 Mt (Figure S6 in Supporting Information S1).

Using the same approach as for SO_2, we find 5.4 ± 1.0 Mt of CO_2 were released in La Palma during the 2021 eruption when assuming degassing of the 0.25 km^3 of erupted volume (Figure 10b). These are minimum values for CO_2, as any volatile emissions from magma which ascended to shallower reservoirs but did not erupt would not be accounted for using this method. We note that our calculated values are five times lower than other previously published values, which find 28 ± 14 Mt of CO_2 emitted for the 2021 eruption based on plume CO_2/SO_2 ratios and solubility modeling (Burton et al., 2023) (Figure 10b). Assuming the same CO_2 concentrations as found in melt inclusions and matrix glasses, we find that degassing ∼1.25 km^3 of magma is needed to release 27.0 ± 5.1 Mt of CO_2 to align with the estimates of Burton et al. (2023) (Figure 10b), indicating that 80% of magma needed to satisfy this budget did not erupt.

Discrepancies clearly exist among SO_2 and CO_2 emissions during the 2021 eruption, as measured SO_2 values via satellite (Milford et al., 2023) and those of CO_2 from solubility models (Burton et al., 2023) would require degassing of significantly different quantities of magma (<0.25 km^3 for SO_2 vs. ∼1.25 km^3 for CO_2), if they are to be directly compared. If five times the measured eruptive volume, or 1.25 km^3, of La Palma 2021 magma degassed, 12.2 ± 2.2 Mt of SO_2, or about five times what was detected via the satellite method (1.84 ± 0.92 Mt SO_2, Milford et al., 2023), would have been emitted (Figure S6 in Supporting Information S1). This indicates that the satellite method (Milford et al., 2023) and petrologic method (Sharma et al., 2004) would severely underestimate SO_2 emissions, or CO_2/SO_2 ratios and solubility modeling (Burton et al., 2023) may overestimate CO_2 emissions if the same amount of magma was unlikely, completely degassed of all volatiles. Each method has weaknesses, with the satellite method not as effective for low-plume altitude eruptions, and the petrographic method unable to account for previously degassed CO_2. Despite these discrepancies, if 28 Mt of CO_2 was released by the 2021 La Palma eruption, it would have accounted for an unexceptional 0.0008% of the 34.9 Gt total global CO_2 emitted in 2021 (Liu et al., 2022), whereas 0.00015% of global CO_2 if the 5.4 ± 1.0 Mt of the petrographic method is correct.

5. Conclusions

- The melt inclusions and olivine host compositions in Tajogaite tephras provide chemical insight into a deep magma chamber filled with an evolving fractionating magma prior to eruption. This pre-eruptive fractionation enriched incompatible volatiles recorded by melt inclusions in low Mg# olivine and allowed cotectic olivine and pyroxene crystallization prior to the eruption. A pulse of primitive magma evidently perturbed this crystallizing deep magma reservoir, recorded by melt inclusions in higher Mg# olivine, leading to the eruption of a mixed crystal record.
- Despite their differences, we find that both melt and fluid inclusions can reliably identify magma storage depths. Though melt inclusions can further elucidate distinct chemical changes in magma source, if rapid magma depth information is needed, fluid inclusions are a more rapid, precise, accurate, and more cost-effective tool to locate previous magma storage levels if they are present within samples.
- We find utility in decrepitated fluid inclusions, and stress that careful petrographic observations can allow their use to identify multiple (shallower) levels of magma storage.

- Complicating melt inclusion work, we find that H_2O contents of melt inclusions within the same olivine population can vary by 1.5 wt% within a single eruption, indicating that previous studies which may have only selected one sample per-eruption may incompletely characterize the diversity of magmatic water contents.
- We note that volatile budgets from petrological, satellite, and ground-based methods are inherently different and must be comprehensively evaluated to understand the true volatile budgets of volcanic eruptions.

Data Availability Statement

All Jupyter notebooks, raw Raman data, TrueMatch Raman phase identification reports, and melt inclusions photos are available in a Zenodo repository at https://doi.org/10.5281/zenodo.10607193 (Dayton et al., 2024) which includes Jupyter notebooks used for DiadFit v0.0.57, v0.0.74, and v0.0.81 (Wieser & DeVitre, 2023), Thermobar v1.0.15 (Wieser et al., 2022), Vesical v1.2.3 (Iacovino et al., 2021), and the Monte Carlo simulation used for volatile budget calculations. Data used for this work are available in Data Set S1. Samples correspond to the following IGSN persistent identifiers: LM0: https://doi.org/10.58052/IEGAZ001I, LM1: https://doi.org/10.58052/IEGAZ001J, LM2: https://doi.org/10.58052/IEGAZ001K, LM3: https://doi.org/10.58052/IEGAZ001L, LM4: https://doi.org/10.58052/IEGAZ001M, LM5: https://doi.org/10.58052/IEGAZ001N, and LM6: https://doi.org/10.58052/IEGAZ001O.

Acknowledgments
This work was funded by NSF Grants EAR 2318614 and 2216738 to EG and 2217371 to PW. VRT acknowledges support from the Swedish Research Council. FJPT and MA thank to the LAJIAL (PGC2018-101027-B-I00, MCIU/AEI/FEDER, EU) and MESVOL (SD RD 1078/2021 LA PALMA) research projects for financial support of their fieldwork. We thank Brian Monteleone and Mike Jercinovic for assistance with SIMS and EPMA analysis. Discussions with Terry Plank, Glenn Gaetani, Sandro Aiuppa, and Paul Wallace improved this manuscript. We thank Jake Lowenstern and Jacqueline Dixon for their thoughtful reviews which improved this manuscript. We are grateful to PEVOLCA for enabling access to the Exclusion Zone of La Palma during the 2021 eruption for sample collection.

References

Aiuppa, A., Bitetto, M., Donne, D. D., LaMonica, F. P., Tamburello, G., Coppola, D., et al. (2021). Volcanic CO_2 tracks the incubation period of basaltic paroxysms. *Science Advances*.

Allison, C. M., Roggensack, K., & Clarke, A. B. (2021). Highly explosive basaltic eruptions driven by CO_2 exsolution. *Nature Communications*, *12*(1), 217. https://doi.org/10.1038/s41467-020-20354-2

Anguita, F., & Hernán, F. (2000). The Canary Islands origin: A unifying model. *Journal of Volcanology and Geothermal Research*, *103*(1–4), 1–26. https://doi.org/10.1016/s0377-0273(00)00195-5

Barker, A. K., Troll, V. R., Carracedo, J. C., & Nicholls, P. A. (2015). The magma plumbing system for the 1971 Teneguía eruption on La Palma, Canary Islands. *Contributions to Mineralogy and Petrology*, *170*(5–6), 54. https://doi.org/10.1007/s00410-015-1207-7

Barth, A., Newcombe, M., Plank, T., Gonnermann, H., Hajimirza, S., Soto, G. J., et al. (2019). Magma decompression rate correlates with explosivity at basaltic volcanoes—Constraints from water diffusion in olivine. *Journal of Volcanology and Geothermal Research*, *387*, 106664. https://doi.org/10.1016/j.jvolgeores.2019.106664

Bonadonna, C., Pistolesi, M., Biass, S., Voloschina, M., Romero, J., Coppola, D., et al. (2022). Physical characterization of long-lasting hybrid eruptions: The 2021 Tajogaite eruption of Cumbre Vieja (La Palma, Canary Islands). *Journal of Geophysical Research: Solid Earth*, *127*(11), e2022JB025302. https://doi.org/10.1029/2022jb025302

Bucholz, C. E., Gaetani, G. A., Behn, M. D., & Shimizu, N. (2013). Post-entrapment modification of volatiles and oxygen fugacity in olivine-hosted melt inclusions. *Earth and Planetary Science Letters*, *374*, 145–155. https://doi.org/10.1016/j.epsl.2013.05.033

Burton, M., Aiuppa, A., Allard, P., Asensio-Ramos, M., Cofrades, A. P., La Spina, A., et al. (2023). Exceptional eruptive CO_2 emissions from intra-plate alkaline magmatism in the Canary volcanic archipelago. *Communications Earth & Environment*, *4*(1), 467. https://doi.org/10.1038/s43247-023-01103-x

Campeny, M., Menendez, I., Ibanez-Insa, J., Rivera-Martinez, J., Yepes, J., Alvarez-Pousa, S., et al. (2023). The ephemeral fumarolic mineralization of the 2021 Tajogaite volcanic eruption (La Palma, Canary Islands, Spain). *Scientific Reports*, *13*(1), 6336. https://doi.org/10.1038/s41598-023-33387-6

Campione, M. (2018). Threshold effects for the decrepitation and stretching of fluid inclusions. *Journal of Geophysical Research: Solid Earth*, *123*(5), 3539–3548. https://doi.org/10.1029/2018jb015694

Campione, M., Malaspina, N., & Frezzotti, M. L. (2015). Threshold size for fluid inclusion decrepitation. *Journal of Geophysical Research: Solid Earth*, *120*(11), 7396–7402. https://doi.org/10.1002/2015jb012086

Canil, D. (2002). Vanadium in peridotites, mantle redox and tectonic environments: Archean to present. *Earth and Planetary Science Letters*, *195*(1–2), 75–90. https://doi.org/10.1016/s0012-821x(01)00582-9

Carracdeo, J. C., Rodriguez Badiola, E., & Soler, V. (1992). The 1730-1736 eruption of Lanzarote, Canary Islands: A long, high-magnitude basaltic fissure eruption. *Journal of Volcanology and Geothermal Research*, *53*(1–4), 239–250. https://doi.org/10.1016/0377-0273(92)90084-q

Carracdeo, J. C., & Troll, V. R. (2016). *The geology of the Canary Islands*. Elsevier. https://doi.org/10.1016/C2015-0-04268-X

Carracedo, J. C. (1994). The Canary Islands: An example of structural control on the growth of large oceanic-island volcanoes. *Journal of Volcanology and Geothermal Research*, *60*(3–4), 225–241. https://doi.org/10.1016/0377-0273(94)90053-1

Carracedo, J. C., Badiola, E. R., Guillou, H., de La Nuez, J., & Perez Torrado, F. J. (2001). Geology and volcanology of la Palma and El Hierro, western Canaries. *Estudios Geologicos-Madrid*, *57*(5–6), 175–273. https://doi.org/10.3989/egeol.01575-6134

Carracedo, J. C., Badiola, E. R., Guillou, H., Paterne, M., Scaillet, S., Torrado, F. J. P., et al. (2007). Eruptive and structural history of Teide Volcano and rift zones of Tenerife, Canary Islands. *Geological Society of America Bulletin*, *119*(9–10), 1027–1051. https://doi.org/10.1130/b26087.1

Carracedo, J. C., Day, S., Guillou, H., RodrÍGuez Badiola, E., Canas, J. A., & Pérez Torrado, F. J. (1998). Hotspot volcanism close to a passive continental margin: The Canary Islands. *Geological Magazine*, *135*(5), 591–604. https://doi.org/10.1017/s0016756898001447

Carracedo, J. C., Guillou, H., Nomade, S., Rodriguez-Badiola, E., Perez-Torrado, F. J., Rodriguez-Gonzalez, A., et al. (2011). Evolution of ocean-island rifts: The northeast rift zone of Tenerife, Canary Islands. *Geological Society of America Bulletin*, *123*(3–4), 562–584. https://doi.org/10.1130/b30119.1

Carracedo, J. C., Troll, V. R., Day, J. M. D., Geiger, H., Aulinas, M., Soler, V., et al. (2022). The 2021 eruption of the Cumbre Vieja volcanic ridge on La Palma Canary Islands. *Geology Today*, *38*(3), 94–107. https://doi.org/10.1111/gto.12388

Cashman, K. V., Sparks, R. S., & Blundy, J. D. (2017). Vertically extensive and unstable magmatic systems: A unified view of igneous processes. *Science*, *355*(6331). https://doi.org/10.1126/science.aag3055

Civico, R., Ricci, T., Scarlato, P., Taddeucci, J., Andronico, D., Del Bello, E., et al. (2022). High-resolution digital surface model of the 2021 eruption deposit of Cumbre Vieja volcano, La Palma, Spain. *Scientific Data*, *9*(1), 435. https://doi.org/10.1038/s41597-022-01551-8

Danyushevsky, L. V., Della-Dasqua, F. N., & Sokolov, S. (2000). Re-equilibration of melt inclusions trapped by magnesian olivine phenocrysts from subduction-related magmas: Petrological implications. *Contributions to Mineralogy and Petrology*, *138*(1), 68–83. https://doi.org/10.1007/pl00007664

D'Auria, L., Koulakov, I., Prudencio, J., Cabrera-Perez, I., Ibanez, J. M., Barrancos, J., et al. (2022). Rapid magma ascent beneath La Palma revealed by seismic tomography. *Scientific Reports*, *12*(1), 17654. https://doi.org/10.1038/s41598-022-21818-9

Day, J. M. D., & Hilton, D. R. (2020). Heterogeneous mantle-derived helium isotopes in the Canary Islands and other ocean islands. *Geology*, *49*(2), 120–124. https://doi.org/10.1130/g47676.1

Day, J. M. D., Pearson, D. G., Macpherson, C. G., Lowry, D., & Carracedo, J.-C. (2009). Pyroxenite-rich mantle formed by recycled oceanic lithosphere: Oxygen-osmium isotope evidence from Canary Island lavas. *Geology*, *37*(6), 555–558. https://doi.org/10.1130/g25613a.1

Day, J. M. D., Pearson, D. G., Macpherson, C. G., Lowry, D., & Carracedo, J. C. (2010). Evidence for distinct proportions of subducted oceanic crust and lithosphere in HIMU-type mantle beneath El Hierro and La Palma, Canary Islands. *Geochimica et Cosmochimica Acta*, *74*(22), 6565–6589. https://doi.org/10.1016/j.gca.2010.08.021

Day, J. M. D., Troll, V. R., Aulinas, M., Deegan, F. M., Geiger, H., Carracedo, J. C., et al. (2022). Mantle source characteristics and magmatic processes during the 2021 La Palma eruption. *Earth and Planetary Science Letters*, *597*, 117793. https://doi.org/10.1016/j.epsl.2022.117793

Dayton, K., Gazel, E., Wieser, P., Troll, V. R., Carracedo, J. C., La Madrid, H., et al. (2023). Deep magma storage during the 2021 La Palma eruption. *Science Advances*, *9*(6). https://doi.org/10.1126/sciadv.ade7641

Dayton, K., Gazel, E., Wieser, P. E., Troll, V. R., Carracedo, J. C., Aulinas, M., & Perez-Torrado, F. J. (2024). Data for volatile constraints of the 2021 La Palma eruption (LaPalma_MI_v0.1.0) [Dataset]. *Zenodo*. https://doi.org/10.5281/zenodo.10607193

Delcamp, A., Troll, V. R., van Wyk de Vries, B., Carracedo, J. C., Petronis, M. S., Pérez-Torrado, F. J., & Deegan, F. M. (2012). Dykes and structures of the NE rift of Tenerife, Canary Islands: A record of stabilisation and destabilisation of ocean island rift zones. *Bulletin of Volcanology*, *74*(5), 963–980. https://doi.org/10.1007/s00445-012-0577-1

Del Fresno, C., Cesca, S., Klugel, A., Dominguez Cerdena, I., Diaz-Suarez, E. A., Dahm, T., et al. (2023). Magmatic plumbing and dynamic evolution of the 2021 La Palma eruption. *Nature Communications*, *14*(1), 358. https://doi.org/10.1038/s41467-023-35953-y

De Luca, C., Valerio, E., Giudicepietro, F., Macedonio, G., Casu, F., & Lanari, R. (2022). Pre- and co-eruptive analysis of the September 2021 eruption at Cumbre Vieja volcano (La Palma, Canary Islands) through DInSAR measurements and analytical modeling. *Geophysical Research Letters*, *49*(7), e2021GL097293. https://doi.org/10.1029/2021gl097293

DeVitre, C. L., Allison, C. M., & Gazel, E. (2021). A high-precision CO_2 densimeter for Raman spectroscopy using a fluid density calibration apparatus. *Chemical Geology*, *584*, 120522. https://doi.org/10.1016/j.chemgeo.2021.120522

DeVitre, C. L., Dayton, K., Gazel, E., Wieser, P., Pamukçu, A., & Gaetani, G. (2023). Laser heating effect on Raman analysis of CO_2 co-existing as liquid and vapor in olivine-hosted melt inclusion bubbles. *Volcanica*, *6*(2), 201–219. https://doi.org/10.30909/vol.06.02.201219

DeVitre, C. L., Gazel, E., Ramalho, R. S., Venugopal, S., Steele-MacInnis, M., Hua, J., et al. (2023). Oceanic intraplate explosive eruptions fed directly from the mantle. *Proceedings of the National Academy of Sciences of the United States of America*, *120*(33), e2302093120. https://doi.org/10.1073/pnas.2302093120

Dietterich, H. R., Diefenbach, A. K., Soule, S. A., Zoeller, M. H., Patrick, M. P., Major, J. J., & Lundgren, P. R. (2021). Lava effusion rate evolution and erupted volume during the 2018 Kīlauea lower East Rift Zone eruption. *Bulletin of Volcanology*, *83*(4), 25. https://doi.org/10.1007/s00445-021-01443-6

Duan, Z., & Zhang, Z. (2006). Equation of state of the H_2O, CO_2, and H_2O–CO_2 systems up to 10 GPa and 2573.15K: Molecular dynamics simulations with ab initio potential surface. *Geochimica et Cosmochimica Acta*, *70*(9), 2311–2324. https://doi.org/10.1016/j.gca.2006.02.009

Duggen, S., Hoernle, K. A., Hauff, F., Klügel, A., Bouabdellah, M., & Thirlwall, M. F. (2009). Flow of Canary mantle plume material through a subcontinental lithospheric corridor beneath Africa to the Mediterranean. *Geology*, *37*(3), 283–286. https://doi.org/10.1130/g25426a.1

Esposito, R., Klebesz, R., Bartoli, O., Klyukin, Y., Moncada, D., Doherty, A., & Bodnar, R. (2012). Application of the Linkam TS1400XY heating stage to melt inclusion studies. *Open Geosciences*, *4*(2), 208–218. https://doi.org/10.2478/s13533-011-0054-y

Esse, B., Burton, M., Hayer, C., Pfeffer, M. A., Barsotti, S., Theys, N., et al. (2023). Satellite derived SO_2 emissions from the relatively low-intensity, effusive 2021 eruption of Fagradalsfjall, Iceland. *Earth and Planetary Science Letters*, *619*, 118325. https://doi.org/10.1016/j.epsl.2023.118325

Fabbrizio, A., Bamber, E. C., Michailidou, E., Romero, J. E., Arzilli, F., Bonechi, B., et al. (2023). Phase equilibrium experiments and thermodynamic simulations to constrain the pre-eruptive conditions of the 2021 Tajogaite eruption (Cumbre Vieja volcano, La Palma, Canary Islands). *Journal of Volcanology and Geothermal Research*, *442*, 107901. https://doi.org/10.1016/j.jvolgeores.2023.107901

Fernandez, J., Escayo, J., Camacho, A. G., Palano, M., Prieto, J. F., Hu, Z., et al. (2022). Shallow magmatic intrusion evolution below La Palma before and during the 2021 eruption. *Scientific Reports*, *12*(1), 20257. https://doi.org/10.1038/s41598-022-23998-w

Ferriss, E., Plank, T., Newcombe, M., Walker, D., & Hauri, E. (2018). Rates of dehydration of olivines from San Carlos and Kilauea Iki. *Geochimica et Cosmochimica Acta*, *242*, 165–190. https://doi.org/10.1016/j.gca.2018.08.050

Gaetani, G. A., O'Leary, J. A., Shimizu, N., Bucholz, C. E., & Newville, M. (2012). Rapid reequilibration of H_2O and oxygen fugacity in olivine-hosted melt inclusions. *Geology*, *40*(10), 915–918. https://doi.org/10.1130/g32992.1

Gaston, C., Barkley, A., Royer, H., Hope, E., Prospero, J. M., Panechou, K., et al. (2022). Comparing the impact of African dust, biomass burning, and volcanic ash on marine and terrestrial biogeochemical cycles. In *AGU fall meeting 2022*.

Geldmacher, J., Hoernle, K., Bogaard, P. V. D., Duggen, S., & Werner, R. (2005). New $^{40}Ar/^{39}Ar$ age and geochemical data from seamounts in the Canary and Madeira volcanic provinces: Support for the mantle plume hypothesis. *Earth and Planetary Science Letters*, *237*(1–2), 85–101. https://doi.org/10.1016/j.epsl.2005.04.037

Ghiorso, M. S., & Gualda, G. A. R. (2015). An H_2O–CO_2 mixed fluid saturation model compatible with rhyolite-MELTS. *Contributions to Mineralogy and Petrology*, *169*(6), 53. https://doi.org/10.1007/s00410-015-1141-8

Gisbert, G., Troll, V. R., Day, J. M. D., Geiger, H., Perez-Torrado, F. J., Aulinas, M., et al. (2023). Reported ultra-low lava viscosities from the 2021 La Palma eruption are potentially biased. *Nature Communications*, *14*(1), 6453. https://doi.org/10.1038/s41467-023-42022-x

Goldstein, R. H., & Reynolds, T. J. (1994). Systematics of fluid inclusions in diagenetic minerals. *SEPM Society for Sedimentary Geology*, *31*.

Gonzalez-Garcia, D., Boulesteix, T., Klugel, A., & Holtz, F. (2023). Bubble-enhanced basanite-tephrite mixing in the early stages of the Cumbre Vieja 2021 eruption, La Palma, Canary Islands. *Scientific Reports*, *13*(1), 14839. https://doi.org/10.1038/s41598-023-41595-3

Hanyu, T., Yamamoto, J., Kimoto, K., Shimizu, K., & Ushikubo, T. (2020). Determination of total CO_2 in melt inclusions with shrinkage bubbles. *Chemical Geology*, *557*, 119855. https://doi.org/10.1016/j.chemgeo.2020.119855

Hartley, M. E., Shorttle, O., Maclennan, J., Moussallam, Y., & Edmonds, M. (2017). Olivine-hosted melt inclusions as an archive of redox heterogeneity in magmatic systems. *Earth and Planetary Science Letters*, *479*, 192–205. https://doi.org/10.1016/j.epsl.2017.09.029

Hartley, M. E., Waters, E. C., Burgess, R., Burton, M., Halldorsson, S. A., Pankhurst, M., et al. (2022). Halogens in melt inclusions trace recycled mantle lithologies. In *2022 Goldschmidt conference*.

Hauri, E. (2002). SIMS analysis of volatiles in silicate glasses, 2: Isotopes and abundances in Hawaiian melt inclusions. *Chemical Geology*, *183*(1–4), 115–141. https://doi.org/10.1016/s0009-2541(01)00374-6

Hofmann, A. W. (2007). Sampling mantle heterogeneity through oceanic basalts: Isotopes and trace elements. In *Treatise on geochemistry* (pp. 1–44). https://doi.org/10.1016/b0-08-043751-6/02123-x

Hornby, A., Gazel, E., Bush, C., Dayton, K., & Mahowald, N. (2023). Phases in fine volcanic ash. *Scientific Reports*, *13*(1), 15728. https://doi.org/10.1038/s41598-023-41412-x

Iacovino, K., Matthews, S., Wieser, P. E., Moore, G. M., & Bégué, F. (2021). VESIcal Part I: An open-source thermodynamic model engine for mixed volatile (H_2O-CO_2) solubility in silicate melts. *Earth and Space Science*, *8*(11). https://doi.org/10.1029/2020ea001584

Iacovino, K., & Till, C. B. (2019). DensityX: A program for calculating the densities of magmaticliquids up to 1,627°C and 30 kbar. *Volcanica*, *2*(1), 1–10. https://doi.org/10.30909/vol.02.01.0110

Kent, A. J. R. (2008). Melt inclusions in basaltic and related volcanic rocks. *Reviews in Mineralogy and Geochemistry*, *69*(1), 273–331. https://doi.org/10.2138/rmg.2008.69.8

Kern, C., Lerner, A. H., Elias, T., Nadeau, P. A., Holland, L., Kelly, P. J., et al. (2020). Quantifying gas emissions associated with the 2018 rift eruption of Kīlauea Volcano using ground-based DOAS measurements. *Bulletin of Volcanology*, *82*(7), 55. https://doi.org/10.1007/s00445-020-01390-8

King, S. D., & Ritsema, J. (2000). African hot spot volcanism: Small-scale convection in the upper mantle beneath cratons. *Science*, *290*(5494), 1137–1140. https://doi.org/10.1126/science.290.5494.1137

Kirstein, L. A., Walowski, K. J., Jones, R. E., Burgess, R., Fitton, J. G., De Hoog, J. C. M., et al. (2023). Volatiles and intraplate magmatism: A variable role for carbonated and altered oceanic lithosphere in ocean island basalt formation. *Journal of Petrology*, *64*(5). https://doi.org/10.1093/petrology/egad022

Klügel, A., Hoernle, K. A., Schmincke, H.-U., & White, J. D. L. (2000). The chemically zoned 1949 eruption on La Palma (Canary Islands): Petrologic evolution and magma supply dynamics of a rift zone eruption. *Journal of Geophysical Research*, *105*(B3), 5997–6016. https://doi.org/10.1029/1999jb900334

Koleszar, A. M., Saal, A. E., Hauri, E. H., Nagle, A. N., Liang, Y., & Kurz, M. D. (2009). The volatile contents of the Galapagos plume; evidence for H_2O and F open system behavior in melt inclusions. *Earth and Planetary Science Letters*, *287*(3–4), 442–452. https://doi.org/10.1016/j.epsl.2009.08.029

Lafuente, B., Downs, R. T., Yang, H., & Stone, N. (2015). The power of databases: The RRUFF project. *Highlights in Mineralogical Crystallography*, 1–30.

Le Bas, M. J., Le Maitre, R. W., Streckeisen, A., & Zanettin, B. (1986). A chemical classification of volcanic rocks based on the total alkali-silica diagram. *Journal of Petrology*, *27*(3), 745–750. https://doi.org/10.1093/petrology/27.3.745

Lerner, A. H., Wallace, P. J., Shea, T., Mourey, A. J., Kelly, P. J., Nadeau, P. A., et al. (2021). The petrologic and degassing behavior of sulfur and other magmatic volatiles from the 2018 eruption of Kīlauea, Hawai'i: Melt concentrations, magma storage depths, and magma recycling. *Bulletin of Volcanology*, *83*(6), 43. https://doi.org/10.1007/s00445-021-01459-y

Le Voyer, M., Asimow, P. D., Mosenfelder, J. L., Guan, Y., Wallace, P. J., Schiano, P., et al. (2014). Zonation of H_2O and F concentrations around melt inclusions in olivines. *Journal of Petrology*, *55*(4), 685–707. https://doi.org/10.1093/petrology/egu003

Liu, Z., Deng, Z., Davis, S. J., Giron, C., & Ciais, P. (2022). Monitoring global carbon emissions in 2021. *Nature Reviews Earth & Environment*, *3*(4), 217–219. https://doi.org/10.1038/s43017-022-00285-w

Lloyd, A. S., Plank, T., Ruprecht, P., Hauri, E. H., & Rose, W. (2012). Volatile loss from melt inclusions in pyroclasts of differing sizes. *Contributions to Mineralogy and Petrology*, *165*(1), 129–153. https://doi.org/10.1007/s00410-012-0800-2

Longpré, M.-A. (2021). Reactivation of Cumbre Vieja volcano. *Science*, *374*(6572), 1197–1198. https://doi.org/10.1126/science.abm9423

Longpré, M.-A., & Felpeto, A. (2021). Historical volcanism in the Canary Islands; part 1: A review of precursory and eruptive activity, eruption parameter estimates, and implications for hazard assessment. *Journal of Volcanology and Geothermal Research*, *419*, 107363. https://doi.org/10.1016/j.jvolgeores.2021.107363

Longpré, M.-A., Stix, J., Klügel, A., & Shimizu, N. (2017). Mantle to surface degassing of carbon- and sulphur-rich alkaline magma at El Hierro, Canary Islands. *Earth and Planetary Science Letters*, *460*, 268–280. https://doi.org/10.1016/j.epsl.2016.11.043

López, C., Blanco, M. J., Abella, R., Brenes, B., Cabrera Rodríguez, V. M., Casas, B., et al. (2012). Monitoring the volcanic unrest of El Hierro (Canary Islands) before the onset of the 2011-2012 submarine eruption. *Geophysical Research Letters*, *39*(13), L13303. https://doi.org/10.1029/2012gl051846

Lowenstern, J. B. (1995). Applications of silicate-melt inclusions to the study of magmatic volatiles. *Mineralogical Association of Canada Short Course*, *23*, 71–99.

Maclennan, J. (2017). Bubble formation and decrepitation control the CO_2 content of olivine-hosted melt inclusions. *Geochemistry, Geophysics, Geosystems*, *18*(2), 597–616. https://doi.org/10.1002/2016gc006633

Maclennan, J., McKenzie, D., Grönvold, K., Shimizu, N., Eiler, J. M., & Kitchen, N. (2003). Melt mixing and crystallization under Theistareykir, northeast Iceland. *Geochemistry, Geophysics, Geosystems*, *4*(11), 8624. https://doi.org/10.1029/2003GC000558

Manjón-Cabeza Córdoba, A., & Ballmer, M. D. (2022). The role of edge-driven convection in the generation of volcanism—Part 2: Interaction with mantle plumes, applied to the Canary Islands. *Solid Earth*, *13*(10), 1585–1605. https://doi.org/10.5194/se-13-1585-2022

Martí, J., Pinel, V., López, C., Geyer, A., Abella, R., Tárraga, M., et al. (2013). Causes and mechanisms of the 2011-2012 El Hierro (Canary Islands) submarine eruption. *Journal of Geophysical Research: Solid Earth*, *118*(3), 823–839. https://doi.org/10.1002/jgrb.50087

Martínez-Martínez, J., Mediato, J. F., Mata, M. P., Ordóñez, B., del Moral, B., Bellido, E., et al. (2023). Early fumarolic minerals from the Tajogaite volcanic eruption (La Palma, 2021). *Journal of Volcanology and Geothermal Research*, *435*, 107771. https://doi.org/10.1016/j.jvolgeores.2023.107771

McDonough, W. F., & Sun, S. (1995). The composition of the Earth. *Chemical Geology*, *120*(253), 223–253. https://doi.org/10.1016/0009-2541(94)00140-4

Metrich, N., & Wallace, P. J. (2008). Volatile abundances in basaltic magmas and their degassing paths tracked by melt inclusions. *Reviews in Mineralogy and Geochemistry*, *69*(1), 363–402. https://doi.org/10.2138/rmg.2008.69.10

Milford, C., Torres, C., Vilches, J., Gossman, A. K., Weis, F., Suarez-Molina, D., et al. (2023). Impact of the 2021 La Palma volcanic eruption on air quality: Insights from a multidisciplinary approach. *Science of the Total Environment*, *869*, 161652. https://doi.org/10.1016/j.scitotenv.2023.161652

Mironov, N. L., Tobelko, D. P., Smirnov, S. Z., Portnyagin, M. V., & Krasheninnikov, S. P. (2020). Estimation of CO_2 content in the gas phase of melt inclusions using Raman spectroscopy: Case study of inclusions in olivine from the Karymsky volcano (Kamchatka). *Russian Geology and Geophysics*, *61*(5–6), 600–610. https://doi.org/10.15372/RGG2019169

Moore, L. R., Gazel, E., & Bodnar, R. J. (2021). The volatile budget of Hawaiian magmatism: Constraints from melt inclusions from Haleakala volcano, Hawaii. *Journal of Volcanology and Geothermal Research*, *410*, 107144. https://doi.org/10.1016/j.jvolgeores.2020.107144

Moore, L. R., Gazel, E., Tuohy, R., Lloyd, A. S., Esposito, R., Steele-MacInnis, M., et al. (2015). Bubbles matter: An assessment of the contribution of vapor bubbles to melt inclusion volatile budgets. *American Mineralogist*, *100*(4), 806–823. https://doi.org/10.2138/am-2015-5036

Moussallam, Y., Longpré, M.-A., McCammon, C., Gomez-Ulla, A., Rose-Koga, E. F., Scaillet, B., et al. (2019). Mantle plumes are oxidised. *Earth and Planetary Science Letters*, *527*, 115798. https://doi.org/10.1016/j.epsl.2019.115798

Negredo, A. M., van Hunen, J., Rodríguez-González, J., & Fullea, J. (2022). On the origin of the Canary Islands: Insights from mantle convection modelling. *Earth and Planetary Science Letters*, *584*, 117506. https://doi.org/10.1016/j.epsl.2022.117506

Nicklas, R. W., Hahn, R. K. M., Willhite, L. N., Jackson, M. G., Zanon, V., Arevalo, R., & Day, J. M. D. (2022). Oxidized mantle sources of HIMU- and EM-type ocean island basalts. *Chemical Geology*, *602*, 120901. https://doi.org/10.1016/j.chemgeo.2022.120901

Nikogosian, I. K., Elliott, T., & Touret, J. L. R. (2002). Melt evolution beneath thick lithosphere: A magmatic inclusion study of La Palma, Canary Islands. *Chemical Geology*, *183*(1–4), 169–193. https://doi.org/10.1016/s0009-2541(01)00387-4

Pankhurst, M. J., Scarrow, J. H., Barbee, O. A., Hickey, J., Coldwell, B. C., Rollinson, G. K., et al. (2022). Rapid response petrology for the opening eruptive phase of the 2021 Cumbre Vieja eruption, La Palma, Canary Islands. *Volcanica*, *5*(1), 1–10. https://doi.org/10.30909/vol.05.01.0110

Pearce, J. A., & Norry, M. J. (1979). Petrogenetic implications of Ti, Zr, Y, and Nb variations in volcanic rocks. *Contributions to Mineralogy and Petrology*, *69*(1), 33–47. https://doi.org/10.1007/bf00375192

Portnyagin, M., Almeev, R., Matveev, S., & Holtz, F. (2008). Experimental evidence for rapid water exchange between melt inclusions in olivine and host magma. *Earth and Planetary Science Letters*, *272*(3–4), 541–552. https://doi.org/10.1016/j.epsl.2008.05.020

Putirka, K. D. (2008). Thermometers and barometers for volcanic systems. *Reviews in Mineralogy and Geochemistry*, *69*(1), 61–120. https://doi.org/10.2138/rmg.2008.69.3

Ranero, C. R., Torne, M., & Banda, E. (1995). Gravity and multichannel seismic reflection constraints on the lithospheric structure of the Canary Swell. *Marine Geophysical Researches*, *17*(6), 519–534. https://doi.org/10.1007/bf01204342

Rasmussen, D. J., Plank, T. A., Roman, D. C., Power, J. A., Bodnar, R. J., & Hauri, E. H. (2018). When does eruption run-up begin? Multi-disciplinary insight from the 1999 eruption of Shishaldin volcano. *Earth and Planetary Science Letters*, *486*, 1–14. https://doi.org/10.1016/j.epsl.2018.01.001

Rasmussen, D. J., Plank, T. A., Wallace, P. J., Newcombe, M. E., & Lowenstern, J. B. (2020). Vapor-bubble growth in olivine-hosted melt inclusions. *American Mineralogist*, *105*(12), 1898–1919. https://doi.org/10.2138/am-2020-7377

Roedder, E. (1979). Origin and significance of magmatic inclusions. *Bulletin de Mineralogie*, *102*(5), 487–510. https://doi.org/10.3406/bulmi.1979.7299

Romero, J. E., Burton, M., Cáceres, F., Taddeucci, J., Civico, R., Ricci, T., et al. (2022). The initial phase of the 2021 Cumbre Vieja ridge eruption (Canary Islands): Products and dynamics controlling edifice growth and collapse. *Journal of Volcanology and Geothermal Research*, *431*, 107642. https://doi.org/10.1016/j.jvolgeores.2022.107642

Rose-Koga, E. F., Bouvier, A. S., Gaetani, G. A., Wallace, P. J., Allison, C. M., Andrys, J. A., et al. (2021). Silicate melt inclusions in the new millennium: A review of recommended practices for preparation, analysis, and data presentation. *Chemical Geology*, *570*, 120145. https://doi.org/10.1016/j.chemgeo.2021.120145

Sandoval-Velasquez, A., Rizzo, A. L., Casetta, F., Ntaflos, T., Aiuppa, A., Alonso, M., et al. (2023). The noble gas signature of the 2021 Tajogaite eruption (La Palma, Canary Islands). *Journal of Volcanology and Geothermal Research*, *443*, 107928. https://doi.org/10.1016/j.jvolgeores.2023.107928

Sharma, K., Blake, S., Self, S., & Krueger, A. J. (2004). SO_2 emissions from basaltic eruptions, and the excess sulfur issue. *Geophysical Research Letters*, *31*(13), L13612. https://doi.org/10.1029/2004gl019688

Shishkina, T. A., Botcharnikov, R. E., Holtz, F., Almeev, R. R., Jazwa, A. M., & Jakubiak, A. A. (2014). Compositional and pressure effects on the solubility of H_2O and CO_2 in mafic melts. *Chemical Geology*, *388*, 112–129. https://doi.org/10.1016/j.chemgeo.2014.09.001

Span, R., & Wagner, W. (1996). A new equation of state for carbon dioxide covering the fluid region from the triple-point temperature to 1100 K at pressures up to 800 MPa. *Journal of Physical and Chemical Reference Data*, *25*(6), 1509–1596. https://doi.org/10.1063/1.555991

Steele-MacInnis, M., Esposito, R., Moore, L. R., & Hartley, M. E. (2017). Heterogeneously entrapped, vapor-rich melt inclusions record pre-eruptive magmatic volatile contents. *Contributions to Mineralogy and Petrology*, *172*(4), 18. https://doi.org/10.1007/s00410-017-1343-3

Taracsák, Z., Hartley, M. E., Burgess, R., Edmonds, M., Iddon, F., & Longpré, M. A. (2019). High fluxes of deep volatiles from ocean island volcanoes: Insights from El Hierro, Canary Islands. *Geochimica et Cosmochimica Acta*, *258*, 19–36. https://doi.org/10.1016/j.gca.2019.05.020

Taracsák, Z., Longpré, M.-A., Tartèse, R., Burgess, R., Edmonds, M., & Hartley, M. E. (2022). Highly oxidising conditions in volatile-rich El Hierro magmas: Implications for ocean island magmatism. *Journal of Petrology*, *63*(3). https://doi.org/10.1093/petrology/egac011

Tenzer, R., Bagherbandi, M., & Vajda, P. (2013). Global model of the upper mantle lateral density structure based on combining seismic and isostatic models. *Geosciences Journal*, *17*(1), 65–73. https://doi.org/10.1007/s12303-013-0009-z

Thirlwall, M. F., Jenkins, C., Vroon, P. Z., & Mattey, D. P. (1997). Crustal interaction during construction of ocean islands: Pb Sr Nd O isotope geochemistry of the shield basalts of Gran Canaria, Canary Islands. *Chemical Geology*, *135*(3–4), 233–262. https://doi.org/10.1016/s0009-2541(96)00118-0

Torres-González, P. A., Luengo-Oroz, N., Lamolda, H., D'Alessandro, W., Albert, H., Iribarren, I., et al. (2020). Unrest signals after 46 years of quiescence at Cumbre Vieja, La Palma, Canary Islands. *Journal of Volcanology and Geothermal Research*, *392*, 106757. https://doi.org/10.1016/j.jvolgeores.2019.106757

Troll, V. R., & Carracedo, J. C. (2016). Chapter 3- The geology of La Palma. In V. R. Troll, & J. C. Carracedo (Eds.), *The geology of the Canary Islands* (pp. 101–180). Elsevier. https://doi.org/10.1016/b978-0-12-809663-5.00009-8

Ubide, T., Márquez, Á., Ancochea, E., Huertas, M. J., Herrera, R., Coello-Bravo, J. J., et al. (2023). Discrete magma injections drive the 2021 La Palma eruption. *Science Advances*, *9*(27). https://doi.org/10.1126/sciadv.adg4813

Valade, S., Ley, A., Massimetti, F., D'Hondt, O., Laiolo, M., Coppola, D., et al. (2019). Towards global volcano monitoring using multisensor sentinel missions and artificial intelligence: The MOUNTS monitoring system. *Remote Sensing*, *11*(13), 1528. https://doi.org/10.3390/rs11131528

Venugopal, S., Schiavi, F., Moune, S., Bolfan-Casanova, N., Druitt, T., & Williams-Jones, G. (2020). Melt inclusion vapour bubbles: The hidden reservoir for major and volatile elements. *Scientific Reports*, *10*(1), 9034. https://doi.org/10.1038/s41598-020-65226-3

Wallace, P. J., Kamenetsky, V. S., & Cervantes, P. (2015). Melt inclusion CO_2 contents, pressures of olivine crystallization, and the problem of shrinkage bubbles. *American Mineralogist*, *100*(4), 787–794. https://doi.org/10.2138/am-2015-5029

Walowski, K. J., Kirstein, L. A., De Hoog, J. C. M., Elliott, T. R., Savov, I. P., & Jones, R. E. (2019). Investigating ocean island mantle source heterogeneity with boron isotopes in melt inclusions. *Earth and Planetary Science Letters*, *508*, 97–108. https://doi.org/10.1016/j.epsl.2018.12.005

Wanamaker, B. J., Wong, T.-F., & Evans, B. (1990). Decrepitation and crack healing of fluid inclusions in San Carlos olivine. *Journal of Geophysical Research*, *95*(B10), 15623–15641. https://doi.org/10.1029/JB095iB10p15623

Wieser, P. E., & DeVitre, C. L. (2023). DiadFit: An open-sourcePython3 tool for peak fitting of Raman data from silicate melts and CO_2 fluids. https://doi.org/10.31223/X5CQ1F

Wieser, P. E., Lamadrid, H., Maclennan, J., Edmonds, M., Matthews, S., Iacovino, K., et al. (2021). Reconstructing magma storage depths for the 2018 Kīlauean eruption from melt inclusion CO_2 contents: The importance of vapor bubbles. *Geochemistry, Geophysics, Geosystems*, *22*(2), e2020GC009364. https://doi.org/10.1029/2020gc009364

Wieser, P. E., Petrelli, M., Lubbers, J., Wieser, E., Özaydin, S., Kent, A. J. F., & Till, C. B. (2022). Thermobar: An open-source Python3 tool for thermobarometry and hygrometry. *Volcanica*, *5*(2), 349–384. https://doi.org/10.30909/vol.05.02.349384

Yoshimura, S. (2023). Carbon dioxide and water in the crust. Part 1: Equation of state for the fluid. *Journal of Mineralogical and Petrological Sciences*, *118*(1), 221224a. https://doi.org/10.2465/jmps.221224a

Zaczek, K., Troll, V. R., Cachao, M., Ferreira, J., Deegan, F. M., Carracedo, J. C., et al. (2015). Nannofossils in 2011 El Hierro eruptive products reinstate plume model for Canary Islands. *Scientific Reports*, *5*(1), 7945. https://doi.org/10.1038/srep07945

References From the Supporting Information

Beattie, P. (1993). Olivine-melt and orthopyroxene-melt equilibria. *Contributions to Mineralogy and Petrology*, *115*(1), 103–111. https://doi.org/10.1007/bf00712982

Canil, D. (1997). Vanadium partitioning and the oxidation state of Archaean komatiite magmas. *Nature*, *389*(6653), 842–845. https://doi.org/10.1038/39860

Danyushevsky, L. V., & Plechov, P. (2011). Petrolog3: Integrated software for modeling crystallization processes. *Geochemistry, Geophysics, Geosystems*, *12*(7), Q07021. https://doi.org/10.1029/2011gc003516

Dixon, J. E. (1997). Degassing of alkalic basalts. *American Mineralogist*, *82*(3–4), 368–378. https://doi.org/10.2138/am-1997-3-415

Herzberg, C., & O'Hara, M. J. (2002). Plume-associated ultramafic magmas of phanerozoic age. *Journal of Petrology*, *43*(10), 1857–1883. https://doi.org/10.1093/petrology/43.10.1857

Iacono-Marziano, G., Morizet, Y., Le Trong, E., & Gaillard, F. (2012). New experimental data and semi-empirical parameterization of H_2O–CO_2 solubility in mafic melts. *Geochimica et Cosmochimica Acta*, *97*, 1–23. https://doi.org/10.1016/j.gca.2012.08.035

Iacovino, K. (2021). Ferric/ferrous, Fe3+/FeT, fO2 converter (Kress and Carmichael, 1991) (3.2). *Zenodo*. https://doi.org/10.5281/zenodo.5907844

Iacovino, K. (2022). *Calculate fO2 buffer (1.5)*. Zenodo. https://doi.org/10.5281/zenodo.7387196

Jochum, K. P., Nohl, U., Herwig, K., Lammel, E., Stoll, B., & Hofmann, A. W. (2005). GeoReM: A new geochemical database for reference materials and isotopic standards. *Geostandards and Geoanalytical Research*, *29*(3), 333–338. https://doi.org/10.1111/j.1751-908X.2005.tb00904.x

Kelley, K. A., Plank, T., Ludden, J., & Staudigel, H. (2003). Composition of altered oceanic crust at ODP Sites 801 and 1149. *Geochemistry, Geophysics, Geosystems*, *4*(6), 8910. https://doi.org/10.1029/2002gc000435

Kress, V. C., & Carmichael, I. S. E. (1988). Stoichiometry of the iron oxidation reaction in silicate melts. *American Mineralogist*, *73*(11–12), 1267–1274.

Kress, V. C., & Carmichael, I. S. E. (1991). The compressibility of silicate liquids containing Fe_2O_3 and the effect of composition, temperature, oxygen fugacity and pressure on their redox states. *Contributions to Mineralogy and Petrology*, *108*(1–2), 82–92. https://doi.org/10.1007/bf00307328

Lamadrid, H. M., Moore, L. R., Moncada, D., Rimstidt, J. D., Burruss, R. C., & Bodnar, R. J. (2017). Reassessment of the Raman CO_2 densimeter. *Chemical Geology*, *450*, 210–222. https://doi.org/10.1016/j.chemgeo.2016.12.034

Lange, R. A., & Carmichael, I. S. E. (1987). K_2O-CaO-MgO-FeO-Fe_2O_3-Al_2O_3-TiO_2-SiO_2 liquids: New measurements and derived partial molar properties. *Geochimica et Cosmochimica Acta*, *51*(11), 2931–2946. https://doi.org/10.1016/0016-7037(87)90368-1

Lowenstern, J. B. (2000). A review of the contrasting behavior of two magmatic volatiles: Chlorine and carbon dioxide. *Journal of Geochemical Exploration*, *69–70*, 287–290. https://doi.org/10.1016/s0375-6742(00)00075-3

Newman, S., & Lowenstern, J. B. (2002). VolatileCalc: A silicate melt–H_2O–CO_2 solution model written in Visual Basic for excel. *Computers & Geosciences*, *28*(5), 597–604. https://doi.org/10.1016/s0098-3004(01)00081-4

Paton, C., Hellstrom, J., Paul, B., Woodhead, J., & Hergt, J. (2011). Iolite: Freeware for the visualisation and processing of mass spectrometric data. *Journal of Analytical Atomic Spectrometry*, *26*(12), 2508. https://doi.org/10.1039/c1ja10172b

Roeder, R. L., & Emslie, R. F. (1970). Olivine-liquid equilibrium. *Contributions to Mineralogy and Petrology*, *29*(4), 275–289. https://doi.org/10.1007/bf00371276

Stroncik, N. A., Klügel, A., & Hansteen, T. H. (2008). The magmatic plumbing system beneath El Hierro (Canary Islands): Constraints from phenocrysts and naturally quenched basaltic glasses in submarine rocks. *Contributions to Mineralogy and Petrology*, *157*(5), 593–607. https://doi.org/10.1007/s00410-008-0354-5

Webb, P. C., Thompson, M., Potts, P. J., & Wilson, S. A. (2011). *GeoPT29—An international proficiency test for analytical geochemistry laboratories—Report on round 29 (Nephelinite, NKT-1)/June 2011*. International Associatino of Geoanalysts Report, GeoPT29. Retrieved from https://www.geoanalyst.org/wp-content/uploads/2017/10/GeoPT29ReportX.pdf

Wieser, P. E., Jenner, F., Edmonds, M., Maclennan, J., & Kunz, B. E. (2020). Chalcophile elements track the fate of sulfur at Kīlauea Volcano, Hawai'i. *Geochimica et Cosmochimica Acta*, *282*, 245–275. https://doi.org/10.1016/j.gca.2020.05.018

Wulff-Pedersen, E., Neumann, E.-R., & Jensen, B. B. (1996). The upper mantle under La Palma, Canary Islands: Formation of Si−K−Na-rich melt and its importance as a metasomatic agent. *Contributions to Mineralogy and Petrology*, *125*(2–3), 113–139. https://doi.org/10.1007/s004100050210

10.1029/2024GC011491

Erratum

The originally published version of this article contained typographical errors. In the first sentence of the second paragraph of Section 1.1, the value "106 m^3" should be changed to "10^6 m^3" in all instances. In the second sentence of the first paragraph of Section 3, "M Mg#" should be changed to "Mg#." In Column CI, "Canil Equation 1 ΔNNO," of worksheet S8 of the supporting information data set, the values should be shifted up one cell. The errors have been corrected, and this may be considered the authoritative version of record.